Journal Pre-proof

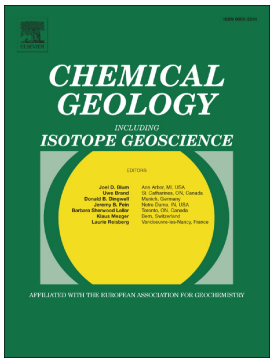

Insights into the REY inventory of seep carbonates from the Northern Norwegian margin using geochemical screening

Katharina Schier, Tobias Himmler, Aivo Lepland, Dennis Kraemer, Jasmin Schönenberger, Michael Bau

PII: S0009-2541(20)30396-X

DOI: https://doi.org/10.1016/j.chemgeo.2020.119857

Reference: CHEMGE 119857

To appear in: *Chemical Geology*

Received date: 27 May 2020

Revised date: 25 August 2020

Accepted date: 26 August 2020

Please cite this article as: K. Schier, T. Himmler, A. Lepland, et al., Insights into the REY inventory of seep carbonates from the Northern Norwegian margin using geochemical screening, *Chemical Geology* (2020), https://doi.org/10.1016/j.chemgeo.2020.119857

Insights into the REY inventory of seep carbonates from the Northern Norwegian margin using geochemical screening

Katharina Schier[a]*, Tobias Himmler[b, c], Aivo Lepland[b, c, d, e], Dennis Kraemer[a], Jasmin Schönenberger[b], and Michael Bau[a]

[a]*Department of Physics and Earth Sciences, Jacobs University Bremen, Campus Ring 1, 28759 Bremen, Germany*

[b]*Geological Survey of Norway, 7491 Trondheim, Norway*

[c]*Centre for Arctic Gas Hydrate, Environment and Climate, Arctic University of Norway (UiT), Tromsø, Norway*

[d]*Department of Geology, Tallinn University of Technology, Tallinn, Estonia*

[e]*Department of Geology, University of Tartu, Ravila 14A, 50411 Tartu, Estonia*

** corresponding author, tel.: +49 421 200 3053, E-Mail address: k.schier@jacobs-university.de (Katharina Schier)*

ABSTRACT

Rare earth element and yttrium (REY) systematics of authigenic seep carbonates can provide insights into the physicochemical characteristics of seep systems and allow discrimination of carbonate precipitation under seawater- or porewater-dominated fluid regimes. However, care must be taken when interpreting their REY systematics, since seep carbonates comprise a mixture of detrital silicates and authigenic carbonate cement. Since concentrations of trace elements, including Rb, Zr, Th and REY, are considerably lower in the carbonate fraction than in the detrital silicate fraction, leaching of these trace elements from detrital components (particularly aluminosilicates) even during a rather "mild" sample decomposition approach with,

for example, nitric acid (HNO_3) can effectively mask the authigenic carbonate REY signal. To assess this effect, trace element concentrations were determined in seep carbonates and detrital sediments from two sites off the Norwegian margin (Lofoten-Vesterålen margin and Vestnesa Ridge). Seep carbonate samples included bulk crusts and nodules, and individual microfacies (microcrystalline aragonite and/or Mg-calcite cementing detrital sediment and void-filling fibrous aragonite cement) microdrilled from crusts. A screening procedure based on Rb, Zr, Th and REY reveals effective masking of the carbonate REY systematics by leaching of trace elements from even minute amounts (0.1-1%) of detrital components. The latter cause elevated trace element concentrations and flat shale-normalized REY patterns. They are prominent in the bulk crusts and nodules, and in microcrystalline carbonate cementing sediment microfacies, which makes these unsuitable as archives of the REY inventory of the carbonate-precipitating fluid even when digested with HNO_3. Some void-filling cements, however, contain little detrital material and show REY signatures characterized by light REY-depletion in shale-normalized (subscript SN) patterns and small negative Ce_{SN} anomalies.

Comparison of the seep carbonate REY_{SN} patterns with seawater and seep porewater REE_{SN} patterns indicate that the detrital contribution considerably masks putative pore water REY_{SN} patterns of microcrystalline carbonate cement. Seawater-like REY_{SN} patterns of void-filling fibrous cements, however, agree with precipitation of this microfacies in an open system dominated largely by seawater near the sediment-water-interface.

Keywords: Rare earth elements, methane seeps, seep carbonates, geochemical screening, trace elements, leaching

1 INTRODUCTION

Methane seeps occur along continental margins where reducing methane-rich fluids escape from

hydrocarbon reservoirs at depth, migrate upwards along faults and fractures, and eventually emanate at the seafloor into the water column (Suess, 2014). Based on geophysical and hydroacoustic data, numerous methane seeps have been found and studied along the Norwegian continental margin (e.g., Hustoft et al., 2009; Mau et al., 2017; Mazzini et al., 2005). Steep geochemical gradients at such methane seeps provide ecological niches for microbial communities mediating the anaerobic oxidation of methane (AOM; Boetius et al., 2000; Reeburgh, 2007), coupling it to either sulfate reduction (Boetius et al., 2000) or the reduction of Fe-(oxyhydr)oxides or Mn-oxides (Beal et al., 2009). A consequence of AOM is the production of bicarbonate (HCO_3^-), resulting in increased pore fluid alkalinity that induces the precipitation of authigenic seep carbonates (e.g., Aloisi et al., 2002; Greinert et al., 1987). Depending on the methane flux and the environmental conditions during carbonate precipitation, seep carbonates comprise variable proportions of aragonite, calcite and dolomite cements (e.g., Aloisi et al., 2002; Greinert et al., 2001; Luff et al., 2004; Naehr et al., 2007; Tong et al., 2019). Aragonite cements typically form mm- to cm-thick linings within open voids, whereas calcite and dolomite mostly occur as microcrystalline cement filling the pore space of detrital seafloor sediments which mainly consist of quartz, feldspar and clay minerals (Greinert et al., 2001; Naehr et al., 2007; Tong et al., 2019). The distribution of the different mineral assemblages between microcrystalline matrix and fibrous cement are not necessarily always the same. In some cases, the microcrystalline matrix may also comprise aragonite and the fibrous cement can be calcite or dolomite.

Carbonate precipitation at methane seeps promotes local sediment lithification and formation of extensive seafloor authigenic carbonate crusts (e.g., Aloisi et al., 2002; Liebetrau et al., 2010; Römer et al., 2014). Geochemical and isotopic characteristics, such as C and O isotope

compositions and Th-U systematics of the crusts provide information for reconstructing sources of emanating fluids and seepage histories (e.g., Aloisi et al., 2002, 2000; Bayon et al., 2013; Crémière et al., 2016, 2013; Hu et al., 2014; Luff et al., 2004; Magalhães et al., 2012; Naehr et al., 2007; Peckmann et al., 2001; Peckmann and Thiel, 2004; Pierre et al., 2014; Ritger et al., 1987; Roberts et al., 2010; Watanabe et al., 2008; Zwicker et al., 2018). Rare earth elements and yttrium (REY) distributions in seep carbonates have also been applied as proxies for discriminating between fluid sources (i.e. seawater vs. porewater) and redox-conditions during carbonate precipitation (e.g., Crémière et al., 2016; Feng et al., 2009; Himmler et al., 2010; Novikova et al., 2015; Rongemaille et al., 2011). Shale-normalized (subscript SN; shale = European Shale of Bau et al., 2018) REY distributions of modern oxic seawater are typically characterized by light REY_{SN} ($LREY_{SN}$) depletion relative to the heavy REY_{SN} ($HREY_{SN}$), positive La_{SN} and Gd_{SN} anomalies, a distinct negative anomaly of redox-sensitive Ce, and a positive Y_{SN} anomaly, i.e. a super-chondritic Y/Ho ratio (e.g., Alibo and Nozaki, 1999; Douville et al., 2002; Elderfield, 1988; Sholkovitz et al., 1994). In contrast, REY_{SN} distributions of pore fluids can differ significantly from those of modern oxic seawater and display much higher REY concentrations and often but not always lack an anomaly of redox-sensitive Ce (Abbott et al., 2015; Deng et al., 2017; Haley et al., 2004; Himmler et al., 2013; Kim et al., 2012; Paul et al., 2019b, 2019a; Soyol-Erdene and Huh, 2013). Reductive dissolution of Fe-oxides in the sediment may release REY with a distinct enrichment of the middle REY (MREY) in their shale-normalized patterns (Haley et al., 2004; Himmler et al., 2010), while reduction of Mn-oxides does not significantly contribute to the REY budget of pore waters (Haley et al., 2004).

Since REY are incorporated into inorganic carbonates without significant fractionation (Nothdurft et al., 2004; Palmer, 1985; Terakado and Masuda, 1988; Zhong and Mucci, 1995), the

REY distribution of the carbonate-precipitating fluid is captured by the seep carbonates (Himmler et al., 2013; Rongemaille et al., 2011). Therefore, the REY distribution of authigenic seep carbonates can be a valuable geochemical tool to distinguish different fluid sources and to constrain the physico-chemical conditions during carbonate formation.

A prerequisite for the applicability of seep carbonate REY distributions as a geochemical proxy for the physico-chemical environment, however, is an assessment of sample purity, i.e. the verification of the absence of significant contributions from detrital (alumino)silicates that can mask the authigenic carbonate REY signal. Seep carbonates comprise a mixture of authigenic carbonate cement and silicates of which especially the aluminosilicates are characterized by high concentrations of elements such as aluminum (Al), rubidium (Rb), zirconium (Zr), and thorium (Th), but also of REY. Contribution of even minute amounts of aluminosilicates to the carbonate samples can, therefore, effectively mask the carbonate REY distribution (e.g., Kamber et al., 2014; Rongemaille et al., 2011; Schier et al., 2018; Tostevin et al., 2016; Webb and Kamber, 2000). Therefore, a thorough screening procedure is necessary to identify samples which can serve as reliable geochemical archives of the authigenic carbonate REY distribution.

This study presents trace element data, including REY, for authigenic seep carbonates and for adjacent seep carbonate poor detrital sediments, sampled from two sites at the Norwegian continental margin (Fig. 1). Our study applies a detailed screening procedure for the detrital aluminosilicate contribution in seep carbonates based on the composition of the adjacent detrital sediment. The screening provides insights into the degrees and effects of aluminosilicate contribution and potential trace element leaching from non-carbonate material during sample preparation using nitric acid. It allows to identify the least aluminosilicate-affected samples which can then serve as archives of the authigenic carbonate REY distribution. The assessment

presented here helps to characterize samples most suitable for the interpretation of the environmental conditions during authigenic seep carbonate formation.

2 SAMPLES, METHODS AND ANALYTICAL TECHNIQUES

2.1 Sampling sites

Seep carbonates were collected from two sites at the Norwegian continental margin (Fig. 1), i.e. from the Lofoten-Vesterålen margin (hereafter L-V site; 80 km offshore, 68°9′ N, 10°28′ E, ~750 m water depth; Hong et al., 2019) and from the Vestnesa Ridge (hereafter VR site; 79° N, ~6°54′ E, ~1200 m water depth; Hustoft et al., 2009; Bünz et al., 2012). Samples from the L-V site were collected from two canyons incised into the Lofoten-Vesterålen continental slope. Permeable horizontal sandstone beds of Eocene age are exposed in the canyon walls and serve as conduits for fluid seepage (Hong et al., 2019). U-Th dating of authigenic carbonates from the L-V site suggest protracted seep carbonate formation throughout the last 22 000 years (Hong et al., 2019). The VR site is characterized by active methane seeps at its ridge crest (Bünz et al., 2012; Hustoft et al., 2009; Plaza-Faverola et al., 2015). Uranium-Th dating of seabed and sub-seabed seep carbonates suggest three main episodes of past methane seepage between 160-130 ka, 50-40 ka and 20-5 ka ago (Himmler et al., 2019). Past methane seepage is attributed to fault reactivation and associated methane release due to the waxing and waning of the Svalbard ice sheet (Himmler et al., 2019).

2.2 Sample collection

At the L-V site, carbonate crust and sediment samples (push cores) were collected from the seafloor with the remotely operated vehicle (ROV) Ægir 6000 during R/V G.O. Sars NGU cruise 1710 in 2017 (Fig. 1c; Hong et al., 2019; Sen et al., 2019).

At the VR site, carbonate crusts and nodules were sampled with the ROV from the seafloor and from drill cores intersecting the subsurface down to ~23 meters below seafloor (mbsf). Seafloor carbonate crusts were sampled from metre-scale depressions and mounds within the two up to ~700 m wide actively seeping pockmarks Lunde and Lomvi during the R/V G.O. Sars cruise 1606 in 2016 (Fig. 1b). Subsurface carbonates representing former seafloor crusts were sampled between 5.8 and 21.7 mbsf from two MeBo cores (GeoB21616-1 and GeoB21673-1) drilled within the central Lunde pockmark during expedition MSM57 with R/V Maria S. Merian in 2016 (Fig. 1b; Table 1; Bohrmann et al., 2017; Himmler et al., 2019). Nodular seep carbonates were sampled between 0.1 and 7.5 mbsf from ROV-sampled push cores at Lomvi (P1606-009) and Lunde (P1606-017), and from two gravity cores (GeoB21601-GC02 and GeoB21605-GC04) from Lunde pockmark (Table 1). Carbonate-poor detrital sediment was sampled at various depths from gravity and MeBo drill cores within the pockmarks (Table 1).

2.3 Subsampling procedure

In order to study the REY geochemistry of the authigenic carbonate fraction, four types of samples were taken for geochemical analysis: (1) two types of carbonate microfacies – sampled on a millimeter scale from crust slabs with a handheld microdrill (Figs. 2a, b and 3) – represented by (1a) microcrystalline carbonate cementing detrital sediment (hereafter called microdrilled matrix samples; see Fig. 3 for photomicrographs) and (1b) void-filling fibrous carbonate cement (hereafter called microdrilled fibrous cements; see Fig. 3 for photomicographs); (2) bulk carbonate crusts comprising pulverized cm-sized crust chips including an undefined mixture of matrix and fibrous cement (Figs. 2c, d and 3g, h); (3) bulk carbonate nodules comprising microcrystalline carbonate cementing sediment, i.e. matrix (Fig. 2e, f); and (4) seep carbonate-poor unlithified seafloor sediment sampled from cores adjacent to

the seep carbonates. The sediments represent the detrital endmember; their REY signatures are used to assess the aluminosilicate components present in the seep carbonates and to constrain the degree of contamination of the REY signature of the authigenic carbonate precipitates. All four sample types were analyzed from the VR site, whereas only bulk carbonate crusts and sediments were analyzed from the L-V site.

2.4 Mineralogy

The mineralogical compositions of bulk carbonate crusts (L-V site) and microdrilled microfacies-specific (VR site) samples were determined by X-ray diffraction (XRD) using a BRUKER D8 Advance diffractometer at the Geological Survey of Norway (Cu-Kα radiation; 3 to 75° 2q scanning angle; step size 0.02°, 1 second per step). Minerals were identified by automatic and manual peak search using the BRUKER Diffrac.EVA 3.1 software with ICDD's PDF 4 Minerals database as well as the Crystallographic Open Database. Quantification was performed applying Rietveld refinements with the TOPAS 5 software. Seep carbonate XRD-samples comprised powdered as well as. The uncertainty of mineral quantification is mineral-dependent but generally better than 2 wt%.

2.5 Digestion procedure for trace element analysis

The digestion method applied here uses a 5 M HNO_3 leach which (i) is strong enough to ensure that leached tri- and tetravalent trace elements of interest (e.g., REY) do not re-precipitate or re-adsorb to the residual fraction and are lost during sample decomposition, and (ii) represents the strongest acid previously used in studies investigating trace elements in seep carbonates (e.g. Crémière et al., 2016) in order to quantify the highest possible REY contribution from leaching effects during the applied digestion.

For the 5 M HNO_3 digestion, powders of carbonate and sediment samples were dried for

approximately 12 hours at 110°C. Up to 250 mg (lowest amount: 2.5 mg) of sample powder was digested in 5 M HNO_3 for 2 hours at 60°C in closed acid-cleaned Savillex PTFE vessels on a hotplate. A certified reference material (J-Do1; dolomite CRM, GSJ) was digested along with the carbonate samples for quality control purposes. The digested samples were then filtered using acid-cleaned filter syringes (0.2 µm). The sample solutions were subsequently evaporated to incipient dryness twice and redissolved in 0.5M suprapure HNO_3.

In addition, one sediment sample from the L-V site and two from the VR site were fully digested in a PicoTrace high-temperature high-pressure digestion system (DAS, Bovenden, Germany) at 165 °C overnight using 50 mg of dried sample powder and 3 ml of conc. $HClO_4$ and 3 ml of conc. HF. Sample solutions were evaporated to incipient dryness, redissolved in conc. HCl twice and finally diluted using 0.5 M HNO_3. The reference material SCo-1 (Cody Shale, USGS) was digested along with the samples for quality control. Details regarding this sample digestion procedure are provided in (Dulski, 2001).

Trace elements were analyzed with a PerkinElmer NexION 350X quadrupole ICP-MS at Jacobs University Bremen using standard-sample-bracketing and 2 µg/kg Ru, Re, Rh and Bi as internal standard elements. Interference corrections were implemented using a method modified after Dulski (1994). Uncertainties of ICP-MS measurements are conservatively estimated to be 10% based on results from numerous previous studies. Due to very low REY abundances some samples were further subjected to a column separation/preconcentration technique (Bau et al., 2010) modified after Shabani et al. (1992) and Bau and Dulski (1996a). Anomalies of REY were calculated for shale-normalized data as

$$(La/La^*)_{SN} = La_{SN}/(3Pr_{SN} - 2Nd_{SN}),$$

$$(Ce/Ce^*)_{SN} = Ce_{SN}/(2Pr_{SN} - Nd_{SN}),$$

$(Pr/Pr^*)_{SN} = Pr_{SN}/(0.5Ce_{SN} + 0.5Nd_{SN})$

$(Eu/Eu^*)_{SN} = Eu_{SN}/(0.67Sm_{SN} + 0.33Tb_{SN})$,

$(Gd/Gd^*)_{SN} = Gd_{SN}/(2Tb_{SN} - Dy_{SN})$,

after Bau and Dulski (1996b) and Bolhar et al. (2004).

2.6 Calculation of mixing hyperbolas

For the assessment of carbonate and aluminosilicate fractions, mixing hyperbolas were calculated following the computational approach of Langmuir et al. (1978). This calculation does not require the actual elemental concentrations of endmembers to be known. Instead, it is based on the elemental concentrations of two samples of different composition, which are assumed to have intermediate concentrations between the theoretical endmembers. Consequently, the calculated mixing hyperbola intersects the two sample compositions its calculation is based on and points towards the composition of the potential endmembers.

3 RESULTS

3.1 Petrography and mineralogy

Seafloor crust samples from the L-V site comprise hemipelagic sediment cemented by authigenic Mg-calcite and barite (Hong et al., 2019). Quartz (2-33 wt%), feldspars (up to 3 wt%), and clay minerals (up to 6 wt%) constitute the major non-authigenic minerals. The proportion of authigenic cement phases amounts to 66-98 wt%, with high barite content (up to 86 wt%, Table A.1) in some samples.

Seafloor and carbonates from drill cores of the VR site show brecciated fabrics, comprising relatively early microcrystalline calcite- and aragonite-cemented sediments subsequently cemented by void-filling botryoidal and radial-fibrous aragonite (Himmler et al., 2019). The major non-carbonate phases are quartz (11-18 wt%), plagioclase (up to 6 wt%), and clay

minerals (up to 5 wt%); (Table A.1; Himmler et al., 2019).

Carbonate cemented nodules comprise mainly Mg-calcites, aragonite, and calcite. Quartz, plagioclase and clay minerals are the main non-carbonate minerals. Please note that mineralogical data are not available for all seep carbonate samples analysed in this study.

3.2 Trace elements

3.2.1 Lofoten-Vesterålen site – Bulk carbonate crusts and sediments

Concentrations of trace elements associated with detrital aluminosilicates (e.g., Rb, Zr, and Th) are variable in the HNO_3-digested bulk crust samples, with Rb, Zr and Th concentrations between 1.53 and 26.6 mg/kg, 0.115 and 9.06 mg/kg, and 0.094 and 2.64 mg/kg, respectively (Figs. 4, 5a, b; Table 1 and A.2). All three elements covary, i.e. samples with elevated Rb concentrations also show high Zr and Th concentrations (Fig. 4). Samarium (as a representative of the REY) also shows a positive covariation with Rb and Th (Fig. 5a, b). Total REY concentrations (∑REY) range from 3.20 to 63.9 mg/kg (Table 1 and A.2).

Shale-normalized REY patterns of L-V bulk crust samples show a slight increase from La to Gd and a moderate decrease from Gd to Lu resulting in an overall depletion of the heavy relative to the light REY ($(Yb/Pr)_{SN}$ between 0.61 and 0.78; Fig. 6a; Table A.2) and a slight enrichment of the middle REY_{SN} ($MREY_{SN}$). The samples do not show pronounced anomalies of La_{SN} ($(La/La^*)_{SN}$: 0.84-1.07), Ce_{SN} ($(Ce/Ce^*)_{SN}$: 0.98-1.21), and Gd_{SN} ($(Gd/Gd^*)_{SN}$: 0.95-1.03; Fig. 6a; Table A.2). Y/Ho ratios range between 28.3 and 32.9 (Figs. 6a, 7a-c; Table 1 and A.2). Three samples (*P1710-045*, *-004* and *-038*) yield slightly different REY_{SN} patterns with super-chondritic Y/Ho ratios between 36.0 and 43.5 and total REY concentrations (∑REY: 3.20, 10.4, and 17.6 mg/kg, respectively) below those of the other bulk crust samples (Fig. 6a; Table 1 and A.2). Sample *P1710-045* additionally shows a small positive La_{SN} anomaly ($(La/La^*)_{SN}$: 1.31),

while the other two do not (Table A.2).

The HNO_3-digested L-V sediment samples show Rb, Th and Sm in the same range as the HNO_3-digested bulk crusts with concentrations between 10.9 and 19.8 mg/kg, 1.70 and 3.14 mg/kg, and 1.59 and 2.61 mg/kg, respectively (Figs. 4c, 5a, b; Table 1 and A.2). Total REY concentrations range from 42.6 to 69.2 mg/kg (Table 1 and A.2). Their REY_{SN} patterns are similar to those of the bulk crusts with a lack of La_{SN}, Ce_{SN} Eu_{SN} and Gd_{SN} anomalies ($(La/La^*)_{SN}$: 0.93-1.03, $(Ce/Ce^*)_{SN}$: 1.00-1.07, $(Eu/Eu^*)_{SN}$: 0.94-1.01, $(Gd/Gd^*)_{SN}$: 1.02-1.18) and Y/Ho ratios between 24.2 and 26.1 (Fig. 6a; Table 1 and A.2). The $HClO_4$-HF-digested L-V sediment sample (sample P*1710-16*) shows much higher concentrations of Rb, Zr and Th of 124 mg/kg, 69.4 mg/kg, and 5.62 mg/kg, respectively (Fig. 4), as well as increased Sm, i.e. total REY concentrations of ∑REY = 129 mg/kg (Fig. 5a, b; Table 1 and A.2) relative to HNO_3-digested bulk carbonate crusts and sediments (Fig. 6a). The REY_{SN} pattern of the fully digested L-V sediment is rather flat (Fig. 6a). Its Y/Ho ratio is 26.7, i.e. chondritic (Table 1 and A.2).

3.2.2 Vestnesa Ridge site – Bulk carbonate nodules, microdrilled matrix and sediment

Microdrilled matrix and bulk nodules from the Vestnesa Ridge generally show trace element concentrations similar to bulk crusts and HNO_3-digested sediments of the L-V site. Rubidium, Zr and Th concentrations range from 13.5 to 40.9 mg/kg, 2.70 to 8.17 mg/kg, and 1.10 to 5.70 mg/kg, respectively (Figs. 4, 5; Tables 1, A.2, A.3), with the bulk nodules extending the range of values to the higher elemental concentrations (Fig. 5c, d). Samarium concentrations (0.99-2.38 mg/kg) and ∑REY (32.5-74.0 mg/kg) are also similar in both HNO_3-digested sample sets (Tables 1, A.2, A.3; Fig. 5c, d) with the exception of nodule samples T34, T36 and T38, which show elevated ∑REY of 113 mg/kg, 130 mg/kg and 186 mg/kg, respectively (Table 1 and A.3).

REY_{SN} distributions of VR microdrilled matrix samples are also remarkably similar to those of the L-V bulk carbonate crusts and sediments with a gradual increase from La to Gd and a decrease from Gd to Lu, i.e. a slight $MREY_{SN}$ enrichment (Fig. 6b) resulting in $(Yb/Pr)_{SN}$ between 0.46 and 0.97 (Table A.3). The REY_{SN} patterns are devoid of pronounced anomalies ($(La/La^*)_{SN}$ = 0.78-1.39, $(Ce/Ce^*)_{SN}$ = 0.96-1.22, $(Gd/Gd^*)_{SN}$ = 0.89-1.42, and $(Eu/Eu^*)_{SN}$ = 1.06-1.24). The slightly elevated $(Gd/Gd^*)_{SN}$ in some samples can be attributed to the underestimation of Tb. None of the samples exhibits super-chondritic Y/Ho ratios (Y/Ho = 23.1-27.4; Fig. 7a-c; Table 1 and A.3). Again, bulk nodule samples T36 and T38 are exceptional in that they show higher $(Yb/Pr)_{SN}$ ratios of 1.31 and 1.43 respectively (Table A.3), and the microdrilled matrix sample T01 exhibits a negative Ce_{SN} anomaly with $(Ce/Ce^*)_{SN}$ = 0.71 and a super-chondritic Y/Ho ratio of 40.7 while sample T03 shows no negative Ce anomaly ($(Ce/Ce^*)_{SN}$ = 1.15) and Y/Ho of 36.1 (Table 1 and A.3).

The two $HClO_4$-HF-digested sediment samples from the VR site show Rb, Zr and Th concentrations in the same order of magnitude as the corresponding L-V site sediment, with Rb concentrations of 228 and 176 mg/kg, Zr concentrations of 151 and 159 mg/kg, and Th concentrations of 10.6 and 7.39 mg/kg, respectively (Figs. 4, 5a, b; Table 1 and A.3). REY concentrations in the VR sediment samples (∑REY: 156 and 206 mg/kg; Table 1 and A.3) are higher than those of the VR microdrilled matrix and most of the bulk nodule samples (except for T38) (∑REY: 32.5 to 53.5 mg/kg; Table 1 and A.3; Fig. 6b), but their REY_{SN} patterns are similar, except for the lack of a distinct $HREY_{SN}$ depletion ($(Yb/Pr)_{SN}$: 0.96 and 1.15; Table A.3). They do not show any REY anomalies and close-to-chondritic Y/Ho ratios of 26.4 and 25.8 (Fig. 7b; Table 1 and A.3).

3.2.3 Vestnesa Ridge site – Void-filling fibrous cements

Microdrilled fibrous aragonite cements show overall very low trace element concentrations and larger variability in REY concentrations and REY_{SN} distributions compared to the microdrilled matrix samples. Rubidium, Zr and Th concentrations range from 0.117 to 2.15 mg/kg, from 0.135 to 0.865 mg/kg and 0.0073 to 0.132 mg/kg, respectively (Fig. 5c, d; Table 1 and A.4). Total REY concentrations are an order of magnitude lower than in the VR microdrilled matrix samples (Figs. 5c, d, 6b, c, d), ranging from 0.39 to 4.27 mg/kg (Table 1 and A.4). Some REY_{SN} patterns are $LREY_{SN}$-depleted with $(Yb/Pr)_{SN}$ up to 3.26, along with strongly super-chondritic Y/Ho ratios as high as 62.7 (Figs. 6c, 7d-f; Table 1 and A.4). On the other hand, some samples show relatively high total REY concentrations (see Sm in Figs. 5c, d, 7d; Table 1 and A.4) and rather flat REY_{SN} patterns with $(Yb/Pr)_{SN}$ ratios close to or below unity (e.g., samples *T08, T24, T04*; Fig. 6c; Table A.4).

4 DISCUSSION

4.1 Impact of detrital aluminosilicates

Previous studies on the REY geochemistry of authigenic seep carbonates have commonly applied a single step digestion method with acetic acid or HNO_3 of various strengths (e.g., Crémière et al., 2016; Feng et al., 2009; Himmler et al., 2010; Rongemaille et al., 2011). However, systematic studies on the effects of REY liberation from non-carbonate phases during digestion with HNO_3 demonstrate that leaching of REY and other elements potentially associated with detrital aluminosilicates (e.g., Rb, Zr and Th) may not be negligible, even during partial leaching with 2% HNO_3 or weak acetic acid (Rongemaille et al., 2011; Tostevin et al., 2016). This may lead to a strong masking effect of the authigenic carbonate-hosted REY inventory by detritus-derived REY, depending on the relative proportions of pure carbonate and non-carbonate phases. This masking effect may be reflected by an increase of the $LREY_{SN}$ and the attenuation

of super-chondritic Y/Ho ratios and $(Ce/Ce^*)_{SN}$ anomalies in carbonates carrying a pristine seawater REY_{SN} pattern (Tostevin et al., 2016). Therefore, when interpreting the REY geochemistry of carbonates, a thorough screening procedure needs to be applied to ensure that the targeted carbonate REY content and, therefore, its distribution is not controlled by the presence of leached REY from detrital phases (e.g., Schier et al., 2018). Alternatively, laser ablation (LA) ICP-MS can be applied to target individual carbonate mineral phases with high spatial resolution, omitting the detrital components if the different minerals are not too tightly intergrown. This method was used for example by Himmler et al. (2010) and Smrzka et al. (2016) on different kinds of seep carbonate samples to measure trace element contents, especially REY, in aragonite. However, REY data obtained by LA-ICP-MS often produce less smooth REY patterns than solution ICP-MS due to (very) low REY concentrations. This hampers reliable interpretation of REY patterns and calculation of the respective anomalies. When applying solution ICP-MS on digested sample material – as in our study – leaching effects have to be considered, which requires a detailed screening procedure to identify the samples that are adequate archives of the carbonate-precipitating fluid.

Constraining the detrital aluminosilicate endmember composition represented by the sediments from the respective sites, is of utmost importance to the aforementioned screening procedure. At both the L-V and the VR site, the $HClO_4$-HF-digested sediments are characterized by significantly higher Rb, Zr, Th and REY concentrations than bulk crusts and nodules, microdrilled matrix and fibrous cement samples and show rather flat REY_{SN} patterns (Tables A.2-A.4; Figs. 4, 5, 6a, b). The HNO_3-digested L-V sediments, however, show Rb, Th and Sm concentrations that are in the same range as in the L-V bulk crusts.

Also, the composition of the authigenic carbonate-precipitating fluid needs to be constrained. At

seeps, the carbonate-precipitating fluid is mainly influenced by either seawater or porewater. Whereas seawater REY distributions are well-studied, REY data for porewaters are scarce – especially for methane seeps (Bayon et al., 2011; Himmler et al., 2013) – and do not show uniform characteristics (Abbott et al., 2015; Deng et al., 2017; Paul et al., 2019a, 2019b; Soyol-Erdene and Huh, 2013) since their distribution is governed by the respective biogeochemical processes within the sediment such as Fe-, Mn- and sulfate-reduction.

We therefore approximate the possible REY_{SN} distribution of porewaters near methane seeps by using the average dissolved REE composition of five samples from 0 to 80 cm below seafloor sampled at an active methane seep in the Niger Delta (Bayon et al., 2011). The average seep porewater shows a rather flat REE_{SN} pattern with a positive Ce_{SN} anomaly and a slight $MREY_{SN}$ enrichment (Fig. 6a). In contrast, modern oxic seawater is characterized by a $LREY_{SN}$ depletion, a positive La_{SN} and Gd_{SN} anomaly, a distinct negative Ce_{SN} anomaly and a super-chondritic Y/Ho ratio (e.g., Alibo and Nozaki, 1999; Douville et al., 2002; Sholkovitz et al., 1994; Fig. 6).

Since the pore water REE_{SN} pattern is very similar to that of the sediments sampled for the present study (except for the positive Ce_{SN} anomaly), applying a screening procedure based on detrital indicators (Th, Rb, and REY concentrations) and a specific anomaly characterizing the REY_{SN} pattern of the precipitating fluid would be ineffective due to the lack of distinctive REY_{SN} features of the seep porewater compared to the sediments (Fig. 6a).

In the case of seawater, on the other hand, a screening procedure based on Sm (as a representative of the REY), Rb and Th concentrations (as an indicator of the presence of detrital material) and Y/Ho ratios (super-chondritic values as an indicator of a seawater-like REY distribution) works reasonably well.

4.2 Screening procedure based on detrital indicators and a seawater-like fluid endmember

4.2.1 Lofoten-Vesterålen bulk crust samples

High concentrations of Rb, Th and Sm and a positive covariation of the Sm concentration with Rb (Fig. 5a) and Th abundances (Fig. 5b) in the bulk carbonate crust samples suggest a detrital control of the Sm concentrations and, hence, their entire REY inventory. This is corroborated by the mixing hyperbolas that were calculated using the lowest and highest concentrations of Rb, Sm, Zr and Th in the L-V sample set, respectively (Figs. 4, 5a, b). These mixing hyperbolas give an indication of the composition of a possible endmember, i.e. in this case of the detrital fraction in the samples. Samarium, Rb and Th concentrations of the L-V bulk carbonate crusts plot along the mixing hyperbolas based on the samples *P1710-045* and *P1710-056-17* of the L-V sample set (Fig. 5a, b). These mixing hyperbolas point towards an endmember composition that closely resembles that of the $HClO_4$-HF-digested L-V sediment (Fig. 5a, b).

Consequently, samples with the lowest Rb, Th and REY concentrations show the least impact of detrital aluminosilicates on their REY distribution, which is corroborated by Y/Ho ratios in relation to Sm, Rb, and Th concentration (Fig. 7a-c): Super-chondritic Y/Ho ratios are characteristic of seawater (e.g., Alibo and Nozaki, 1999; Bau et al., 1995) and are shown by samples that show low concentrations of Sm, i.e. REY (Fig. 7a), Rb (Fig. 7b) and Th (Fig. 7c) while quickly approaching chondritic Y/Ho ratios ($(Y/Ho)_{chondrite}$ = 28; Anders and Grevesse, 1989) with increasing Sm, Rb and Th content. Therefore, samples *P1710-045*, *-038* and *-004*, which are the samples with the least aluminosilicate contribution of the L-V bulk carbonates, may point towards a carbonate-precipitating fluid endmember, the composition of which is seawater-like rather than porewater-like. Still, their REY distribution is markedly influenced by detritus-derived REY, as indicated by elevated Rb, Th, and Sm concentrations combined with only “mildly” super-chondritic Y/Ho ratios. Given that REY easily desorb/leach from detritus

during sample digestion with weak nitric acid (Rongemaille et al., 2011; Tostevin et al., 2016), the majority of the carbonate REY in our bulk carbonate crust samples is likely derived from leaching of the detrital fraction with its abundant clay minerals. This obscures the genuine authigenic carbonate REY_{SN} patterns. This is corroborated by the mineralogical composition which reveals trace amounts of plagioclase and kaolinite in the three samples with the least aluminosilicate contribution (Table A.1). The remainder of the L-V bulk crusts shows even higher amounts of detrital clay minerals and, therefore, also a larger detritus imprint on their REY distribution (Figs. 6a, 7a-c).

A comparison of the 5 M HNO_3 and a full $HClO_4$-HF digestion reveals the effect of increased detrital influence: Bulk crust samples that were digested in HNO_3 generally show lower REY concentrations than those that underwent a full acid digestion (Fig. A.1 of the supplementary material). Moreover, samples that show slightly super-chondritic Y/Ho ratios in the HNO_3 digest lose this feature when fully digested, i.e. when the detrital fraction is also dissolved and contributes to the sample's total REY budget (Fig. A.1). Assuming that the REY content of the carbonate fraction in the bulk crusts is almost negligible relative to that of the residual fraction, simple mass balance calculations show that using 5 M HNO_3 liberates more than 32 % of the REY in a sample (Table A.5), underlining that the digestion with 5 M HNO_3 not only attacks the authigenic carbonate phases but also leaches a significant proportion of REY from the residual fraction. Additionally, this is supported by HNO_3-digested L-V sediments which show similar elemental concentrations and REY_{SN} patterns as the L-V bulk crusts (Figs. 4c, 5a, b). Therefore, we consider a leaching effect of the aluminosilicate fraction (best approximated by the HNO_3-digested L-V sediments) in our bulk crust samples to be responsible for the REY_{SN} patterns (Fig. 6a). Because of the significant influence of detrital material on the REY abundances and

distribution of the bulk carbonate crusts digested with 5 M HNO_3, none of the samples is considered a suitable geochemical archive of the REY_{SN} signature of the ambient fluid from which the authigenic carbonate fraction of the bulk samples precipitated. Whether the dominant REY source for the authigenic carbonate fraction of the bulk crust samples was seawater or a diagenetic pore fluid remains, therefore, elusive.

It should also be noted, that not only the digestion with 5 M HNO_3 will result in significant trace element leaching from the detrital fraction as shown here, but digestions applying weaker acids to similar sample material will suffer from the same effect, albeit less pronounced. However, a quantification of the leaching effect using weaker acids is not possible based on the results for a 5 M HNO_3 digestion presented in this work. This would rather require digestions and screening procedures – similar the one presented here – to be conducted with different acid strengths, most preferably those that are commonly used in trace element analysis of seep carbonates (2 to 5% acetic acid and weaker nitric acid strengths than 5 M HNO_3). Nevertheless, we re-emphasize that data determined using weaker acids may suffer from experimental artifacts such as re-precipitation or re-adsorption of analytes.

4.2.2. Vestnesa Ridge bulk nodules and microdrilled matrix samples

Rubidium, Th and Sm concentrations in the VR bulk nodules cover the same range as the microdrilled VR matrix samples (Figs. 5c, d, 7d-f) and their REY_{SN} patterns are very much alike with a few exceptions (*T34*, *T36*, *T38*; Fig. 6b). Their mostly (sub-)chondritic Y/Ho ratios are similar to those of the $HClO_4$-HF-digested VR sediment samples (Fig. 7d-f), indicating that the bulk nodules and the microdrilled matrix samples suffer from the same masking effect with respect to their REY_{SN} patterns as the bulk carbonate crust samples from the L-V site. The microdrilled matrix samples comprise carbonate cemented seafloor sediment. The REY

concentrations in the carbonate cement fraction are very low compared to those of the seafloor sediment (Figs. 6a, b, 7) that mainly consists of clay minerals, plagioclase and quartz. Leaching of the latter during the digestion procedure very likely releases REY (with flat, sediment-like patterns; Fig. 6b), and other elements associated with the detrital fraction of the sample, resulting in effective masking of the carbonate REY_{SN} patterns (e.g., Tostevin et al., 2016). A straightforward interpretation of the authigenic carbonate REY distribution is, therefore, hampered by the aluminosilicate contribution to the VR bulk nodules and microdrilled matrix samples.

Concentrations of Th and Sm as well as the shape of the VR microdrilled matrix REY_{SN} patterns are similar (Figs. 5d, 6b, 7d, f) to previously published data of HNO_3-digested seep carbonate matrix samples from the Alvheim channel (Crémière et al., 2016). Texturally early microcrystalline aragonites of carbonate crusts from the Northern Arabian Sea also show MREY-enriched REY_{SN} patterns with total REY concentrations of 39 to 52 mg/kg (Himmler et al., 2010), which are in the same range as in the VR matrix samples. Both studies attribute the relatively high REY concentrations and non-seawater like, MREY-enriched REY_{SN} patterns of the microcrystalline cement (see Fig. 6b for an exemplary REY_{SN} pattern from Crémière et al. (2016)) to carbonate precipitation from an early diagenetic and possibly anoxic fluid that showed $MREY_{SN}$ enrichment due to the remobilization of MREY during diagenetic processes (Crémière et al., 2016; Himmler et al., 2010). Previous studies on anoxic pore waters from the Peru Basin revealed elevated REY concentrations relative to seawater and a $MREY_{SN}$ bulge in their REY_{SN} patterns due to MREY release during the reduction of Fe(III)-oxides by early diagenetic processes and subsequent incorporation of this $MREY_{SN}$ enrichment in diagenetic carbonate precipitates (Haley et al., 2004; Himmler et al., 2013). A study by Paul et al. (2019a), on the

other hand, revealed seawater-like REY_{SN} patterns in pore waters of the Peru Basin showing that pore water characteristics and elemental distributions are highly heterogeneous at relatively small spatial scales.

However, our screening procedure reveals an alternative explanation for the elevated REY concentrations and the $MREY_{SN}$ enrichment in microcrystalline seep carbonate cement. Since nitric acid was used to digest the microcrystalline carbonate samples, it is likely that a similar leaching effect is responsible for the REY_{SN} patterns described by Crémière et al. (2016) and Himmler et al. (2010).

4.2.3 Vestnesa Ridge microdrilled void-filling fibrous cements

Fibrous cements show much more variable REY_{SN} patterns and lower REY concentrations than the matrix samples (Fig. 6c, d). However, a positive covariation of Sm with detrital indicators (Rb, Th; Fig. 5c, d) and decreasing Y/Ho ratios with increasing Sm, Rb and Th concentrations (Fig. 7d-f) suggest at least a partial control of the REY systematics by detrital material in some of the fibrous cement samples.

To illustrate the impact of a leaching effect by even minute amounts of aluminosilicate minerals on the REY signature of the VR fibrous cements, binary mixing calculations were performed (Fig. 8a, b). We calculated the REY_{SN} patterns of sample T02, assuming the presence of different amounts of aluminosilicates (given in % of the total sample; Fig. 8a). We chose sample T02, because judging from its low Rb and Th concentrations it is a rather pure carbonate and the complete REY pattern is available. For the endmember of the aluminosilicate fraction, REY concentrations and patterns were assumed to be equal to $HClO_4$-HF-digested VR sediment which represents the most likely aluminosilicate contributor to the sample set. The results demonstrate that only 0.1% of aluminosilicates in the total sample would already result in a significant

attenuation of the super-chondritic Y/Ho ratio, a less pronounced $LREY_{SN}$ depletion, and an overall increase in REY concentrations (green REY_{SN} pattern in Fig. 8a). With a share of 1% (brown REY_{SN} pattern in Fig. 8a), all seawater-like characteristics of the carbonate endmember in sample T02 are fully obscured and the REY_{SN} pattern is similar to that of VR background sediment, although REY concentrations are still two orders of magnitude lower (Fig. 8a).

Additionally, the same calculations were performed for sample T02, assuming it had a pronounced negative Ce_{SN} anomaly (Fig. 8b). For this purpose, an artificial negative Ce_{SN} anomaly was implemented, setting the Ce concentration of sample T02 to only 50% of its original value. These mixing calculations demonstrate how a potentially present negative Ce_{SN} anomaly would be obscured by 0.1% and 1 % aluminosilicates in the sample: Like for the Y/Ho ratio, a share of 0.1% significantly suppresses the size of the negative Ce_{SN} anomaly (green REY_{SN} pattern in Fig. 8b) and a share of 1% fully erases it (brown REY_{SN} patterns in Fig. 8b), resulting in a similar REY_{SN} distribution as in the VR background sediment sample but lower concentrations.

However, samples with very low Sm, Rb and Th concentrations, i.e. small detrital contribution, show the highest Y/Ho ratios (Fig. 7d-f) and REY_{SN} patterns that are similar to those of modern seawater with the characteristic $LREY_{SN}$ depletion and super-chondritic Y/Ho ratio (Figs. 6d, 7d-f). Only these samples (*T02*, *T05*, *T20*, *T26*, *T28*, and *T53*) approach the true composition of the precipitating fluid. Hence, these are considered the most reliable geochemical archives that give meaningful insights into the REY composition of their parental fluid and the physico-chemical conditions during their precipitation. Hence, when performed carefully, microdrilling of fibrous cements is a useful technique to gather interpretable seep carbonate REY samples.

4.3 Seawater origin of VR void-filling fibrous cements

The remarkable similarity of REY_{SN} patterns of the purest VR microdrilled fibrous cements (Fig. 6d) with similar cements of Crémière et al. (2016) suggests that fibrous cements of the VR site precipitated most likely under similar conditions and from a parental fluid of similar composition. The seawater-like REY_{SN} patterns with small negative Ce_{SN} anomalies (Fig. 6d; Table A.4) indicate precipitation from a fluid influenced by oxic seawater (Himmler et al., 2010). Assuming that the REY_{SN} pattern of the parental fluid is incorporated into the carbonates without major fractionation (Kamber et al., 2004; Kamber and Webb, 2001; Nothdurft et al., 2004; Van Kranendonk et al., 2003; Webb and Kamber, 2000), this indicates that precipitation of aragonitic fibrous cements in the carbonate crusts of the VR site occurred in rather open conditions with respect to seawater at or very close to the sediment-water interface where the parental fluid (most probably seawater) was negligibly influenced by diagenetic remobilization and enrichment of REY in pore waters (Himmler et al., 2010). Brecciated fabrics (Fig. 2a, b) of the samples and anomalously high $\delta^{18}O$ values indicate past gas hydrate dissolution (see Himmler et al., 2019) and corroborate the implications of their REY geochemistry. This is in line with aragonite precipitation primarily taking place under more open conditions during enhanced methane release, i.e. more vigorous emanation of CH_4-bubbles, at the methane seep site. These conditions enable the entrainment of sulfate-rich seawater (Greinert et al., 2001; Luff et al., 2004) most probably carrying the typical seawater REY_{SN} distribution to the site of aragonite formation, where it is readily captured by the precipitating aragonitic fibrous cements (Crémière et al., 2016; Himmler et al., 2010).

Most recently, Bayon et al. (in press) reported large positive La anomalies in chitinous tubes of siboglinid tube worms (*Escarpia southwardae*) from methane seeps off the coast of West Africa. These unusual La anomalies were attributed to vital effects of aerobic methanotrophs living in

symbiosis with the tube worms. It has been suggested that these symbionts preferentially incorporate LREY – especially La and Ce – utilizing these specific REY as enzymatic cofactors in methanol hydrogenase (e.g., Pol et al., 2014; Roszczenko-Jasińska et al., 2020). Lanthanum anomalies calculated following the quantification used by Bayon et al. (in press) for the purest Vestnesa void-filling aragonite fibrous cements investigated in our study, do not exceed values of 1.3 for (La/La*), i.e. they do not show unusually large positive La anomalies. This suggests that aerobic methanotrophs did not affect the REY distribution recorded by this aragonite.

5 CONCLUSIONS

Seep carbonate crusts from two sampling sites off the Norwegian margin (Lofoten-Vesterålen margin and Vestnesa Ridge) were analyzed for their trace and rare earth element systematics to gain insights into the characteristics of the carbonate-precipitating fluid, i.e. to discriminate between a porewater and a seawater source of the latter. Carbonate crusts at marine methane seeps are mixtures of authigenic carbonate and detrital (alumino)silicate components which show markedly higher concentrations of trace elements like Rb, Zr, Th and REY than the authigenic carbonate fraction. Therefore, the presence of even small amounts of such detrital aluminosilicates may mask the targeted authigenic carbonate REY inventory. A detailed screening procedure based on detrital indicators (e.g., Rb, Th, REY) allows to identify the seep carbonate samples with the least contribution from detrital aluminosilicates and is therefore an essential prerequisite for successfully assessing the REY systematics of the authigenic carbonate fraction. We show that during the applied sample digestion with 5 M HNO_3, significant leaching of elements such as Rb, Th, Zr and also REY from the detrital fraction of a carbonate crust may occur. This leaching effect may not be confined to the digestion method applied here but most likely also occurs when weaker acids are used. It effectively masks the carbonate REY signature

and leads to REY_{SN} patterns controlled by detrital aluminosilicates, even when they are present at very low amounts (< 1%). This compromises the use of such HNO_3-digested aluminosilicate-containing seep carbonate samples as archives of the authigenic carbonate REY inventory. Alternatively, analysis by LA-ICP-MS may circumvent this problem by targeting individual minerals. However, due to low REY concentrations, this usually produces rather irregular REY patterns that are difficult to interpret. Careful microdrilling of aluminosilicate-poor void-filling fibrous aragonite cements produces sample material that is suitable for solution ICP-MS and pure enough to serve as archives of the carbonate-precipitating fluid. Seawater-like REY_{SN} patterns of the Vestnesa Ridge fibrous cements, characterized by $LREY_{SN}$ depletion and small negative Ce_{SN} anomalies, suggest precipitation of such cements from a fluid dominated by seawater, most probably in an open system close to the sediment-water interface. This is consistent with the precipitation of aragonite rather than calcite as void-filling cements during more vigorous emanation of methane bubbles at the seep site.

ACKNOWLEDGEMENTS

Professional support at sea by the masters and crews during expeditions on R/V G.O. Sars (P1710) and R/V Maria S. Merian (MSM57) and the skilful works of the ROV Ægir 6000 team (University of Bergen) and the MARUM-MeBo70 team (University of Bremen) are acknowledged. Further, we appreciate the help of Annika Moje (Jacobs University Bremen) with laboratory work. This study was supported by the Research Council of Norway through Petromaks2-NORCRUST (project 255150) and its Centre of Excellence funding scheme for CAGE (project 223259). We would also like to thank three anonymous reviewers whose contributions significantly improved the first version of this manuscript, and Dr. M. Böttcher for all editorial handling.

REFERENCES

Abbott, A.N., Haley, B.A., McManus, J., Reimers, C.E., 2015. The sedimentary flux of dissolved rare earth elements to the ocean. Geochim. Cosmochim. Acta 154, 186–200. https://doi.org/10.1016/j.gca.2015.01.010

Alibo, D.S., Nozaki, Y., 1999. Rare earth elements in seawater: Particle association, shale-normalization, and Ce oxidation. Geochim. Cosmochim. Acta 63, 363–372. https://doi.org/10.1016/S0016-7037(98)00279-8

Aloisi, G., Bouloubassi, I., Heijs, S., Pancost, R.D., Pierre, C., Sinninghe Damsteé, J.S., Gottschal, J.C., Forney, L.J., Rouchy, J.M., 2002. CH4-consuming microorganisms and the formation of carbonate crusts at cold seeps. Earth Planet. Sci. Lett. 203, 195–203. https://doi.org/10.1016/S0012-821X(02)00872-6

Aloisi, G., Pierre, C., Rouchy, J.M., Foucher, J.P., Woodside, J., 2000. Methane-related authigenic carbonates of Eastern Mediterranean Sea mud volcanoes and their possible relation to gas hydrate destabilisation. Earth Planet. Sci. Lett. 184, 321–338. https://doi.org/10.1016/S0012-821X(00)00322-8

Anders, E., Grevesse, N., 1989. Abundances of the elements: Meteoritic and solar. Geochim. Cosmochim. Acta 53, 197–214. https://doi.org/10.1016/0016-7037(89)90286-X

Bau, M., Balan, S., Schmidt, K., Koschinsky, A., 2010. Rare earth elements in mussel shells of the Mytilidae family as tracers for hidden and fossil high-temperature hydrothermal systems. Earth Planet. Sci. Lett. 299, 310–316. https://doi.org/10.1016/j.epsl.2010.09.011

Bau, M., Dulski, P., 1996a. Anthropogenic origin of positive gadolinium anomalies in river waters. Earth and Planetary Science Letters 143, 245-255.

Bau, M., Dulski, P., 1996b. Distribution of yttrium and rare-earth elements in the Penge and

Kuruman iron-formations, Transvaal Supergroup, South Africa. Precambrian Res. 79, 37–55. https://doi.org/10.1016/0301-9268(95)00087-9

Bau, M., Dulski, P., Möller, P., 1995. Yttrium and holmium in South Pacific seawater: vertical distribution and possible fractionation mechanisms. Chemie der Erde - Geochemistry 55, 1–15. https://doi.org/10.1016/0967-0653(95)95670-0

Bau, M., Schmidt, K., Pack, A., Bendel, V., Kraemer, D., 2018. The European Shale: An improved data set for normalisation of rare earth element and yttrium concentrations in environmental and biological samples from Europe. Appl. Geochemistry 90, 142–149. https://doi.org/10.1016/j.apgeochem.2018.01.008

Bayon, G., Birot, D., Ruffine, L., Caprais, J.-C., Ponzevera, E., Bollinger, C., Donval, J.-P., Charlou, J.-L., Voisset, M., Grimaud, S., 2011. Evidence for intense REE scavenging at cold seeps from the Niger Delta margin. Earth Planet. Sci. Lett. 312, 443–452. https://doi.org/10.1016/j.epsl.2011.10.008

Bayon, G., Dupré, S., Ponzevera, E., Roubleau, J., Chéron, S., Pierre, C., Mascle, J., Boetius, A., De Lange, G.J., 2013. Formation of carbonate chimneys in the Mediterranean Sea linked to deep-water oxygen depletion. Nat. Geosci. 6, 755–760. https://doi.org/10.1038/ngeo1888

Bayon, G., Lemaitre, N., Barrat, J.-A., Wang, X., Feng, D., Duperron, S., (in press). Microbial utilization ofrare earth elements at cold seeps related to aerobic methane oxidation. Chem. Geol. 135601. https://doi.org/doi.org/10.1016/j.chemgeo.2020.119832

Beal, E.J., House, C.H., Orphan, V.J., 2009. Manganese- and iron-dependent marine methane oxidation. Science 325, 184–187. https://doi.org/10.1126/science.1169984

Boetius, A., Ravenschlag, K., Schubert, C.J., Rickert, D., Widdel, F., Gleseke, A., Amann, R., Jørgensen, B.B., Witte, U., Pfannkuche, O., 2000. A marine microbial consortium

apparently mediating anaerobic oxidation methane. Nature 407, 623–626. https://doi.org/10.1038/35036572

Bohrmann, G., Ahrlich, F., Bergenthal, M., Bünz, S., Düßmann, R., Ferreira, C., Freudenthal, T., Fröhlich, S., Hamann, K., Hong, W.-L., Hsu, C.-W., Johnson, J., Kaszemeik, K., Kausche, A., Klein, T., Lange, M., Lepland, A., Malnati, J., Meckel, S., Meyer-Schack, B., Noorlander, K., Panieri, G., Pape, T., Reuter, M., Riedel, M., Rosiak, U., Schmidt, C., Schmidt, W., Seiter, C., Spagnoli, G., Stachowski, A., Stange, M., Wallmann, K., Wintersteller, P., Wunsch, D., Yao, H., 2017. R/V MARIA S. MERIAN Cruise Report MSM57, Gas Hydrate Dynamics at the Continental Margin of Svalbard, Reykjavik–Longyearbyen–Reykjavik, 29 July–07 September 2016.

Bolhar, R., Kamber, B.S., Moorbath, S., Fedo, C.M., Whitehouse, M.J., 2004. Characterisation of early Archaean chemical sediments by trace element signatures. Earth Planet. Sci. Lett. 222, 43–60. https://doi.org/10.1016/j.epsl.2004.02.016

Bünz, S., Polyanov, S., Vadakkepuliyambatta, S., Consolaro, C., Mienert, J., 2012. Active gas venting through hydrate-bearing sediments on the Vestnesa Ridge, offshore W-Svalbard. Mar. Geol. 332–334, 189–197. https://doi.org/10.1016/j.margeo.2012.09.012

Crémière, A., Bayon, G., Ponzevera, E., Pierre, C., 2013. Paleo-environmental controls on cold seep carbonate authigenesis in the Sea of Marmara. Earth Planet. Sci. Lett. 376, 200–211. https://doi.org/10.1016/j.epsl.2013.06.029

Crémière, A., Lepland, A., Chand, S., Sahy, D., Kirsimäe, K., Bau, M., Whitehouse, M.J., Noble, S.R., Martma, T., Thorsnes, T., Brunstad, H., 2016. Fluid source and methane-related diagenetic processes recorded in cold seep carbonates from the Alvheim channel, central North Sea. Chem. Geol. 432, 16–33. https://doi.org/10.1016/j.chemgeo.2016.03.019

Deng, Y., Ren, J., Guo, Q., Cao, J., Wang, H., Liu, C., 2017. Rare earth element geochemistry characteristics of seawater and porewater from deep sea in western Pacific. Sci. Rep. 7, 1–13. https://doi.org/10.1038/s41598-017-16379-1

Douville, E., Charlou, J.L., Oelkers, E.H., Bienvenu, P., Jove Colon, C.F., Donval, J.P., Fouquet, Y., Prieur, D., Appriou, P., 2002. The rainbow vent fluids (36°14′N, MAR): The influence of ultramafic rocks and phase separation on trace metal content in Mid-Atlantic Ridge hydrothermal fluids. Chem. Geol. 184, 37–48. https://doi.org/10.1016/S0009-2541(01)00351-5

Dulski, P., 2001. Reference materials for geochemical studies: New analytical data by ICP-MS and critical discussion of reference values. Geostand. Newsl. 25, 87–125. https://doi.org/10.1111/j.1751-908X.2001.tb00790.x

Dulski, P., 1994. Interferences of oxide, hydroxide and chloride analyte species in the determination of rare earth elements in geological samples by inductively coupled plasma-mass spectrometry. Fresenius. J. Anal. Chem. 350, 194–203. https://doi.org/10.1007/BF00322470

Elderfield, H., 1988. The Oceanic Chemistry of the Rare-Earth Elements. Philos. Trans. R. Soc. A Math. Phys. Eng. Sci. 325, 105–126. https://doi.org/10.1098/rsta.1988.0046

Feng, D., Chen, D., Peckmann, J., 2009. Rare earth elements in seep carbonates as tracers of variable redox conditions at ancient hydrocarbon seeps. Terra Nov. 21, 49–56. https://doi.org/10.1111/j.1365-3121.2008.00855.x

Greinert, J., Bohrmann, G., Suess, E., 2001. Gas hydrate-associated carbonates and methane-venting at hydrate ridge: Classification, distribution, and origin of authigenic lithologies, in: Paull, C.K., Dillon, P.W. (Eds.), Natural Gas Hydrates: Occurrence, Distribution, and

Detection. Geophysical Monograph. pp. 99–113. https://doi.org/10.1029/GM124p0099

Haley, B.A., Klinkhammer, G.P., McManus, J., 2004. Rare earth elements in pore waters of marine sediments. Geochim. Cosmochim. Acta 68, 1265–1279. https://doi.org/10.1016/j.gca.2003.09.012

Himmler, T., Bach, W., Bohrmann, G., Peckmann, J., 2010. Rare earth elements in authigenic methane-seep carbonates as tracers for fluid composition during early diagenesis. Chem. Geol. 277, 126–136. https://doi.org/10.1016/j.chemgeo.2010.07.015

Himmler, T., Haley, B.A., Torres, M.E., Klinkhammer, G.P., Bohrmann, G., Peckmann, J., 2013. Rare earth element geochemistry in cold-seep pore waters of Hydrate Ridge, northeast Pacific Ocean. Geo-Marine Lett. 33, 369–379. https://doi.org/10.1007/s00367-013-0334-2

Himmler, T., Sahy, D., Martma, T., Bohrmann, G., Plaza-Faverola, A., Bünz, S., Condon, D.J., Knies, J., Lepland, A., 2019. A 160,000-year-old history of tectonically controlled methane seepage in the Arctic. Sci. Adv. 5. https://doi.org/10.1126/sciadv.aaw1450

Hong, W.L., Lepland, A., Himmler, T., Kim, J.H., Chand, S., Sahy, D., Solomon, E.A., Rae, J.W.B., Martma, T., Nam, S. Il, Knies, J., 2019. Discharge of Meteoric Water in the Eastern Norwegian Sea since the Last Glacial Period. Geophys. Res. Lett. 46, 8194–8204. https://doi.org/10.1029/2019GL084237

Hu, Y., Feng, D., Peckmann, J., Roberts, H.H., Chen, D., 2014. New insights into cerium anomalies and mechanisms of trace metal enrichment in authigenic carbonate from hydrocarbon seeps. Chem. Geol. 381, 55–66. https://doi.org/10.1016/j.chemgeo.2014.05.014

Hustoft, S., Bünz, S., Mienert, J., Chand, S., 2009. Gas hydrate reservoir and active methane-venting province in sediments on < 20 Ma young oceanic crust in the Fram Strait, offshore

NW-Svalbard. Earth Planet. Sci. Lett. 284, 12–24. https://doi.org/10.1016/j.epsl.2009.03.038

Kamber, B.S., Bolhar, R., Webb, G.E., 2004. Geochemistry of late Archaean stromatolites from Zimbabwe: Evidence for microbial life in restricted epicontinental seas. Precambrian Res. 132, 379–399. https://doi.org/10.1016/j.precamres.2004.03.006

Kamber, B.S., Webb, G.E., 2001. The geochemistry of late Archaean microbial carbonate: Implications for ocean chemistry and continental erosion history. Geochim. Cosmochim. Acta 65, 2509–2525. https://doi.org/10.1016/S0016-7037(01)00613-5

Kamber, B.S., Webb, G.E., Gallagher, M., 2014. The rare earth element signal in Archaean microbial carbonate: Information on ocean redox and biogenicity. J. Geol. Soc. London. 171, 745–763. https://doi.org/10.1144/jgs2013-110

Kim, J.H., Torres, M.E., Haley, B.A., Kastner, M., Pohlman, J.W., Riedel, M., Lee, Y.-J., 2012. The effect of diagenesis and fluid migration on rare earth element distribution in pore fluids of the northern Cascadia accretionary margin. Chem. Geol. 291, 152–165. https://doi.org/10.1016/j.chemgeo.2011.10.010

Langmuir, C.H., Vocke, R.D., Hanson, G.N., Hart, S., 1978. A general mixing equation with applications to icelandic basalts. Earth Planet. Sci. Lett. 37, 380–392.

Liebetrau, V., Eisenhauer, A., Linke, P., 2010. Cold seep carbonates and associated cold-water corals at the Hikurangi Margin, New Zealand: New insights into fluid pathways, growth structures and geochronology. Mar. Geol. 272, 307–318. https://doi.org/10.1016/j.margeo.2010.01.003

Li, Y.H., Schoonmaker, J.E., 2003. Chemical Composition and Mineralogy of Marine Sediments, Treatise on Geochemistry: Second Edition. Elsevier.

https://doi.org/10.1016/B978-0-08-095975-7.00701-4

Luff, R., Wallmann, K., Aloisi, G., 2004. Numerical modeling of carbonate crust formation at cold vent sites: Significance for fluid and methane budgets and chemosynthetic biological communities. Earth Planet. Sci. Lett. 221, 337–353. https://doi.org/10.1016/S0012-821X(04)00107-4

Magalhães, V.H., Pinheiro, L.M., Ivanov, M.K., Kozlova, E., Blinova, V., Kolganova, J., Vasconcelos, C., McKenzie, J.A., Bernasconi, S.M., Kopf, A.J., Díaz-del-Río, V., González, F.J., Somoza, L., 2012. Formation processes of methane-derived authigenic carbonates from the Gulf of Cadiz. Sediment. Geol. 243–244, 155–168. https://doi.org/10.1016/j.sedgeo.2011.10.013

Mau, S., Römer, M., Torres, M.E., Bussmann, I., Pape, T., Damm, E., Geprägs, P., Wintersteller, P., Hsu, C.W., Loher, M., Bohrmann, G., 2017. Widespread methane seepage along the continental margin off Svalbard-from Bjørnøya to Kongsfjorden. Sci. Rep. 7, 1–13. https://doi.org/10.1038/srep42997

Mazzini, A., Aloisi, G., Akhmanov, G.G., Parnell, J., Cronin, B.T., Murphy, P., 2005. Integrated petrographic and geochemical record of hydrocarbon seepage on the Vøring Plateau. J. Geol. Soc. London. 162, 815–827. https://doi.org/10.1144/0016-764904-133

Naehr, T.H., Eichhubl, P., Orphan, V.J., Hovland, M., Paull, C.K., Ussler, W., Lorenson, T.D., Greene, H.G., 2007. Authigenic carbonate formation at hydrocarbon seeps in continental margin sediments: A comparative study. Deep. Res. Part II Top. Stud. Oceanogr. 54, 1268–1291. https://doi.org/10.1016/j.dsr2.2007.04.010

Nothdurft, L.D., Webb, G.E., Kamber, B.S., 2004. Rare earth element geochemistry of Late Devonian reefal carbonates, Canning Basin, Western Australia: Confirmation of a seawater

REE proxy in ancient limestones. Geochim. Cosmochim. Acta 68, 263–283. https://doi.org/10.1016/S0016-7037(03)00422-8

Novikova, S.A., Shnyukov, Y.F., Sokol, E. V., Kozmenko, O.A., Semenova, D. V., Kutny, V.A., 2015. A methane-derived carbonate build-up at a cold seep on the Crimean slope, north-western Black Sea. Mar. Geol. 363, 160–173. https://doi.org/10.1016/j.margeo.2015.02.008

Palmer, M.R., 1985. Rare earth elements in foraminifera tests. Earth Planet. Sci. Lett. 73, 285–298. https://doi.org/10.1016/0012-821X(85)90077-9

Paul, S.A.L., Haeckel, M., Bau, M., Bajracharya, R., Koschinsky, A., 2019a. Small-scale heterogeneity of trace metals including rare earth elements and yttrium in deep-sea sediments and porewaters of the Peru Basin, southeastern equatorial Pacific. Biogeosciences 16, 4829–4849. https://doi.org/10.5194/bg-16-4829-2019

Paul, S.A.L., Volz, J.B., Bau, M., Köster, M., Kasten, S., Koschinsky, A., 2019b. Calcium phosphate control of REY patterns of siliceous-ooze-rich deep-sea sediments from the central equatorial Pacific. Geochim. Cosmochim. Acta 251, 56–72. https://doi.org/10.1016/j.gca.2019.02.019

Peckmann, J., Reimer, A., Luth, U., Luth, C., Hansen, B.T., Heinicke, C., Hoefs, J., Reitner, J., 2001. Methane-derived carbonates and authigenic pyrite from the northwestern Black Sea. Mar. Geol. 177, 129–150. https://doi.org/10.1016/S0025-3227(01)00128-1

Peckmann, J., Thiel, V., 2004. Carbon cycling at ancient methane-seeps. Chem. Geol. 205, 443–467. https://doi.org/10.1016/j.chemgeo.2003.12.025

Pierre, C., Bayon, G., Blanc-Valleron, M.M., Mascle, J., Dupré, S., 2014. Authigenic carbonates related to active seepage of methane-rich hot brines at the Cheops mud volcano, Menes caldera (Nile deep-sea fan, eastern Mediterranean Sea). Geo-Marine Lett. 34, 253–267.

https://doi.org/10.1007/s00367-014-0362-6

Plaza-Faverola, A., Bünz, S., Johnson, J.E., Chand, S., Knies, J., Mienert, J., Franek, P., 2015. Role of tectonic stress in seepage evolution along the gas hydrate-charged Vestnesa Ridge, Fram Strait. Geophys. Res. Lett. 42, 733–742. https://doi.org/10.1002/2014GL062474

Pol, A., Barends, T.R.M., Dietl, A., Khadem, A.F., Eygensteyn, J., Jetten, M.S.M., Op den Camp, H.J.M., 2014. Rare earth metals are essential for methanotrophic life in volcanic mudpots. Environ. Microbiol. 16, 255–264. https://doi.org/10.1111/1462-2920.12249

Reeburgh, W.S., 2007. Oceanic methane biogeochemistry. Chem. Rev. 107, 486–513. https://doi.org/10.1021/cr050362v

Ritger, S., Carson, B., Suess, E., 1987. Methane-derived authigenic carbonates formed by subduction-induced pore-water expulsion along the Oregon/Washington margin. Geol. Soc. Am. Bull. 98, 147–156.

Roberts, H.H., Feng, D., Joye, S.B., 2010. Cold-seep carbonates of the middle and lower continental slope, northern Gulf of Mexico. Deep. Res. Part II Top. Stud. Oceanogr. 57, 2040–2054. https://doi.org/10.1016/j.dsr2.2010.09.003

Römer, M., Sahling, H., Pape, T., dos Santos Ferreira, C., Wenzhöfer, F., Boetius, A., Bohrmann, G., 2014. Methane fluxes and carbonate deposits at a cold seep area of the Central Nile Deep Sea Fan, Eastern Mediterranean Sea. Mar. Geol. 347, 27–42. https://doi.org/10.1016/j.margeo.2013.10.011

Rongemaille, E., Bayon, G., Pierre, C., Bollinger, C., Chu, N.C., Fouquet, Y., Riboulot, V., Voisset, M., 2011. Rare earth elements in cold seep carbonates from the Niger delta. Chem. Geol. 286, 196–206. https://doi.org/10.1016/j.chemgeo.2011.05.001

Roszczenko-Jasińska, P., Vu, H.N., Subuyuj, G.A., Crisostomo, R.V., Cai, J., Lien, N.F.,

Clippard, E.J., Ayala, E.M., Ngo, R.T., Yarza, F., Wingett, J.P., Raghuraman, C., Hoeber, C.A., Martinez-Gomez, N.C., Skovran, E., 2020. Gene products and processes contributing to lanthanide homeostasis and methanol metabolism in Methylorubrum extorquens AM1. Sci. Rep. 10, 12663. https://doi.org/10.1038/s41598-020-69401-4

Schier, K., Bau, M., Münker, C., Beukes, N., Viehmann, S., 2018. Trace element and Nd isotope composition of shallow seawater prior to the Great Oxidation Event: Evidence from stromatolitic bioherms in the Paleoproterozoic Rooinekke and Nelani Formations, South Africa. Precambrian Res. 315, 92–102. https://doi.org/10.1016/j.precamres.2018.07.014

Sen, A., Himmler, T., Hong, W.L., Chitkara, C., Lee, R.W., Ferré, B., Lepland, A., Knies, J., 2019. Atypical biological features of a new cold seep site on the Lofoten-Vesterålen continental margin (northern Norway). Sci. Rep. 9, 1–14. https://doi.org/10.1038/s41598-018-38070-9

Shabani, M.B., Akagi, T., Masuda, A., 1992. Preconcentration of Trace Rare-Earth Elements in Seawater by Complexation with Bis(2-ethylhexyl) Hydrogen Phosphate and 2-Ethylhexyl Dihydrogen Phosphate Adsorbed on a C18 Cartridge and Determination by Inductively Coupled Plasma Mass Spectrometry. Anal. Chem. 64, 737–743. https://doi.org/10.1021/ac00031a008

Sholkovitz, E.R., Landing, W.M., Lewis, B.L., 1994. Ocean particle chemistry: The fractionation of rare earth elements between suspended particles and seawater. Geochim. Cosmochim. Acta 58, 1567–1579. https://doi.org/10.1016/0016-7037(94)90559-2

Smrzka, D., Zwicker, J., Klügel, A., Monien, P., Bach, W., Bohrmann, G., Peckmann, J., 2016. Establishing criteria to distinguish oil-seep from methane-seep carbonates. Geology 44, 667–670. https://doi.org/10.1130/G38029.1

Soyol-Erdene, T.O., Huh, Y., 2013. Rare earth element cycling in the pore waters of the Bering Sea Slope (IODP Exp. 323). Chem. Geol. 358, 75–89. https://doi.org/10.1016/j.chemgeo.2013.08.047

Suess, E., 2014. Marine cold seeps and their manifestations: geological control, biogeochemical criteria and environmental conditions, International Journal of Earth Sciences. https://doi.org/10.1007/s00531-014-1010-0

Terakado, Y., Masuda, A., 1988. The coprecipitation of rare-earth elements with calcite and aragonite. Chem. Geol. 69, 103–110. https://doi.org/10.1016/0009-2541(88)90162-3

Tong, H., Feng, D., Peckmann, J., Roberts, H.H., Chen, L., Bian, Y., Chen, D., 2019. Environments favoring dolomite formation at cold seeps: A case study from the Gulf of Mexico. Chem. Geol. 518, 9–18. https://doi.org/10.1016/j.chemgeo.2019.04.016

Tostevin, R., Shields, G.A., Tarbuck, G.M., He, T., Clarkson, M.O., Wood, R.A., 2016. Effective use of cerium anomalies as a redox proxy in carbonate-dominated marine settings. Chem. Geol. 438, 146–162. https://doi.org/10.1016/j.chemgeo.2016.06.027

Van Kranendonk, M.J., Webb, G.E., Kamber, B.S., 2003. Geological and trace element evidence for a marine sedimentary environment of deposition and biogenicity of 3.45 Ga stromatolitic carbonates in the Pilbara Craton, and support for a reducing Archaean ocean. Geobiology 1, 91–108. https://doi.org/10.1046/j.1472-4669.2003.00014.x

Watanabe, Y., Nakai, S., Hiruta, A., Matsumoto, R., Yoshida, K., 2008. U-Th dating of carbonate nodules from methane seeps off Joetsu, Eastern Margin of Japan Sea. Earth Planet. Sci. Lett. 272, 89–96. https://doi.org/10.1016/j.epsl.2008.04.012

Webb, G.E., Kamber, B.S., 2000. Rare earth elements in Holocene reefal microbialites: A new shallow seawater proxy. Geochim. Cosmochim. Acta 64, 1557–1565.

https://doi.org/10.1016/S0016-7037(99)00400-7

Zhong, S., Mucci, A., 1995. Partitioning of rare earth elements (REEs) between calcite and seawater solutions at 25°C and 1 atm, and high dissolved REE concentrations. Geochim. Cosmochim. Acta 59, 443–453. https://doi.org/10.1016/0016-7037(94)00381-U

Zwicker, J., Smrzka, D., Himmler, T., Monien, P., Gier, S., Goedert, J.L., Peckmann, J., 2018. Rare earth elements as tracers for microbial activity and early diagenesis: A new perspective from carbonate cements of ancient methane-seep deposits. Chem. Geol. 501, 77–85. https://doi.org/10.1016/j.chemgeo.2018.10.010

FIGURE CAPTIONS

Fig. 1: Sampling locations and bathymetry. a) Overview of the sampled locations; asterisks indicate sampled seepage sites (VR = Vestnesa Ridge; L-V = Lofoten-Vesterålen). b) ROV-acquired micro bathymetry of two active pockmarks on Vestnesa Ridge; white triangles = MeBo cores 127 (station GeoB21616-1) and 138 (station GeoB21637-1). c) ROV-acquired micro bathymetry of two canyons off Lofoten islands. a) and b) are modified after Himmler et al. (2019), c) is modified after Hong et al. (2019).

Fig. 2: Photographs of representative seep carbonates. a) to d) Cut slabs of surface crusts sampled from Vestnesa Ridge (a and b) and the Lofoten-Vesterålen site (c and d); respective micro drilled areas (e.g., T57) are highlighted in a) and b); cm-sized chunks were used for bulk-rock analyses for samples c) and d); note skate-egg cases (arrows) in c). e) and f) carbonate nodules sampled from gravity cores and respective bulk-rock trace element samples (e.g., T35). Fig. 2b) is modified after Himmler et al. (2019).

Fig. 3: Photomicrographs of representative seep carbonate textures. a) and b) Scans of epoxy-impregnated slabs of drill core samples (a: sample GeoB21616-2R-1B; b: GeoB21637-12R-2Q) and marked respective micro drilled areas (T05, T06, T21, and T22). c) and d) thin-section micrographs of samples shown in a) and b), respectively; Mic = microcrystalline carbonate

cementing sediment with abundant silt-sized quartz grains; Vfc = void-filling aragonite cement; P = pore space (crossed-polarized light, pore space appears black). e) to h) thin section micrographs of seabed crusts sampled from Vestnesa Ridge (samples e: P1606-002; f: P1606-012) and the Lofoten-Vesterålen site (g: P1710-001; h: P1710-043); parallel-polarized light (i.e. pore space appears bright) in e) and f), cross-polarized light in g) and h); Mic = microcrystalline carbonate cementing sediment; Vfc = void-filling aragonite cement; B = bivalve fragment; P = pore space; note sand-sized quartz grains cemented by microcrystalline carbonate cement (Mic) and authigenic barite (Bar, arrow) in h). Fig. 3a) and b) are modified after Himmler et al. (2019).

Fig. 4: Graphs of detrital indicators – a) Zr vs. Rb, b) Zr vs. Th, and c) Rb vs. Th – for bulk carbonate crusts and sediment from the Lofoten-Vesterålen (L-V) margin, Norway. All graphs also include pelagic clay for comparison (data from Li and Schoonmaker, 2003).

Fig. 5: Graphs of a) Sm as a representative of the REY vs. Rb for bulk carbonate crusts and sediments from the Lofoten-Vesterålen (L-V) margin, b) Sm vs. Th for the same bulk carbonate crusts and sediments, c) Sm vs. Rb for microdrilled matrix and fibrous cement samples, bulk nodules, and sediments from the Vestnesa Ridge (VR), and d) Sm vs. Th for the same samples. d) additionally shows matrix and fibrous cements of carbonate crusts from the Alvheim Channel (data from Crémière et al., 2016). All graphs also include pelagic clay for comparison (data from Li and Schoonmaker, 2003).

Fig. 6: Shale-normalized (shale = European Shale of Bau et al., 2018) REY patterns of a) bulk carbonate crusts and sediments from the Lofoten-Vesterålen (L-V) margin, Norway, and average seep pore water (n = 5) from a cold seep in the Niger delta (average calculated from Bayon et al., 2011), b) of bulk nodules, microdrilled matrix and sediments from the Vestnesa Ridge (VR), Norway, c) all microdrilled fibrous cements from carbonate crusts from the Vestnesa Ridge, and d) fibrous cements with the least impact of detrital aluminosilicates on their REY geochemistry following our screening procedure (for more details see text). A fibrous cement of a carbonate crust from the Alvheim Channel is shown for comparison (data from Crémière et al., 2016). All graphs show a modern seawater REY_{SN} pattern for comparison (data from Alibo and Nozaki, 1999).

Fig. 7: a) Sm vs. Y/Ho ratios for bulk crust samples and sediments from the Lofoten-Vesterålen margin (L-V), Norway, b) Rb vs. Y/Ho ratios, and c) Th vs. Y/Ho ratios for the same samples, d) Sm vs. Y/Ho ratios of bulk nodules, microdrilled matrix samples and fibrous cements from the

Vestnesa Ridge (VR), e) Rb vs. Y/Ho ratios, and f) Th vs. Y/Ho ratios for the same samples. d) and e) also include matrix and fibrous cements of carbonate crusts from the Alvheim Channel (data from Crémière et al., 2016). All graphs include the corresponding sediments for the respective locations, pelagic clay (Li and Schoonmaker, 2003), and the chondritic Y/Ho ratio (C1 data from Anders and Grevesse, 1989).

Fig. 8: Calculated shale-normalized (shale = European Shale from Bau et al., 2018) REY patterns resulting from the mixing of a) a detrital aluminosilicate component (given in % of the sample) represented by Vestnesa Ridge (VR) sediment, and VR fibrous cement sample T02, and b) the same calculated REY_{SN} patterns but with an artificially added negative Ce_{SN} anomaly in the REY_{SN} pattern of T02.

FIGURES

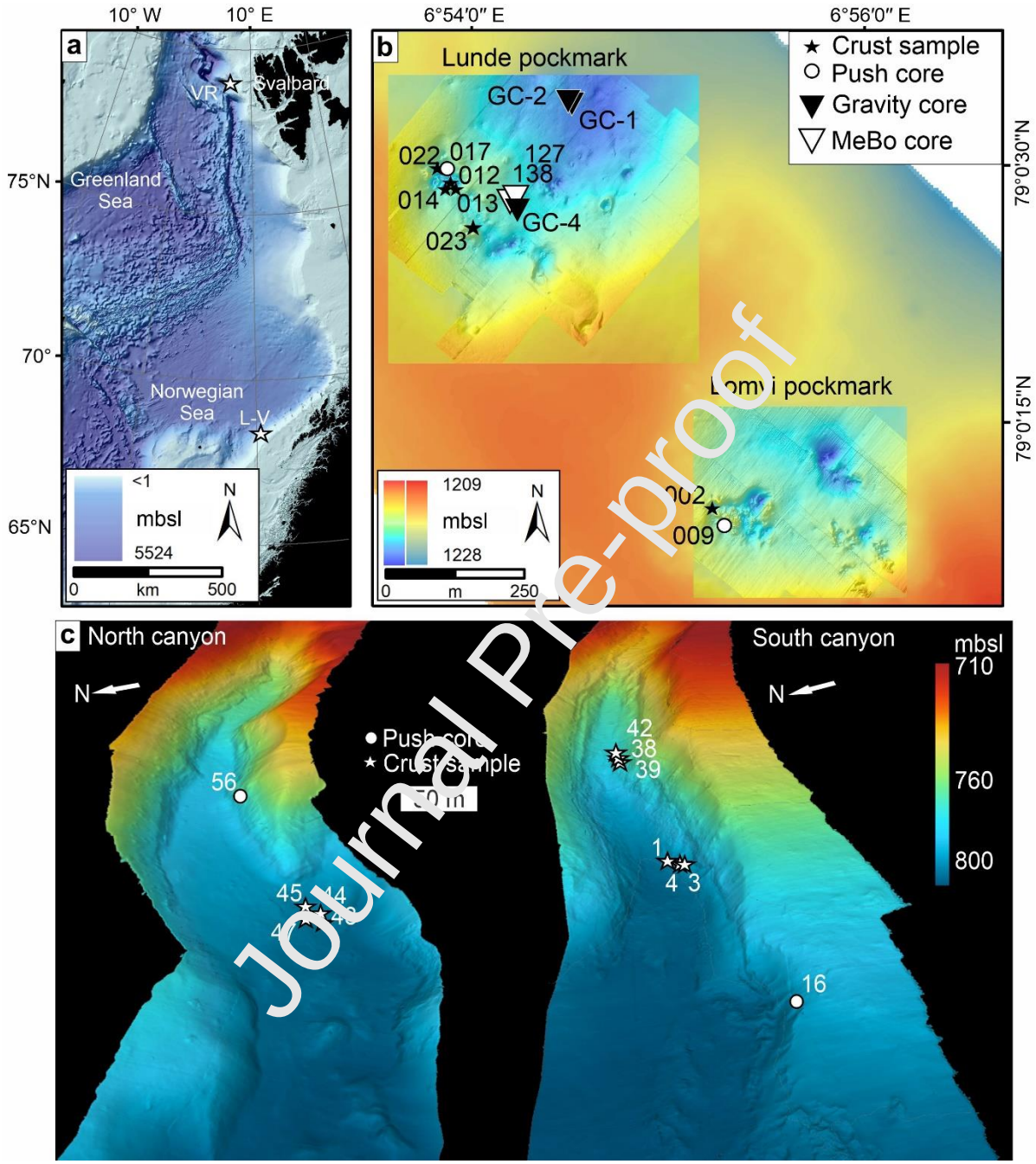

Fig. 1

--- two colum fitting image ---

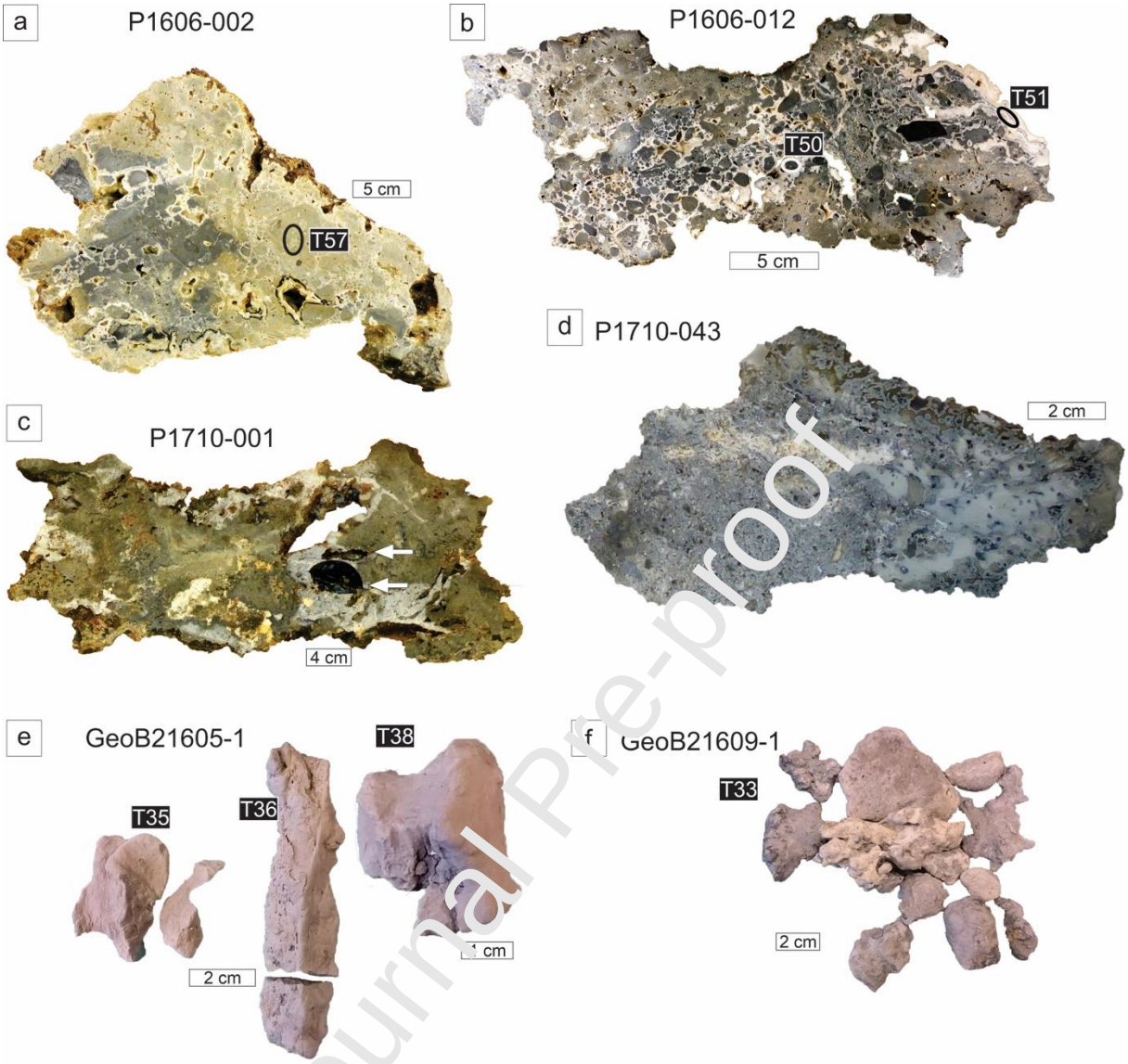

Fig. 2

--- two column fitting image ---

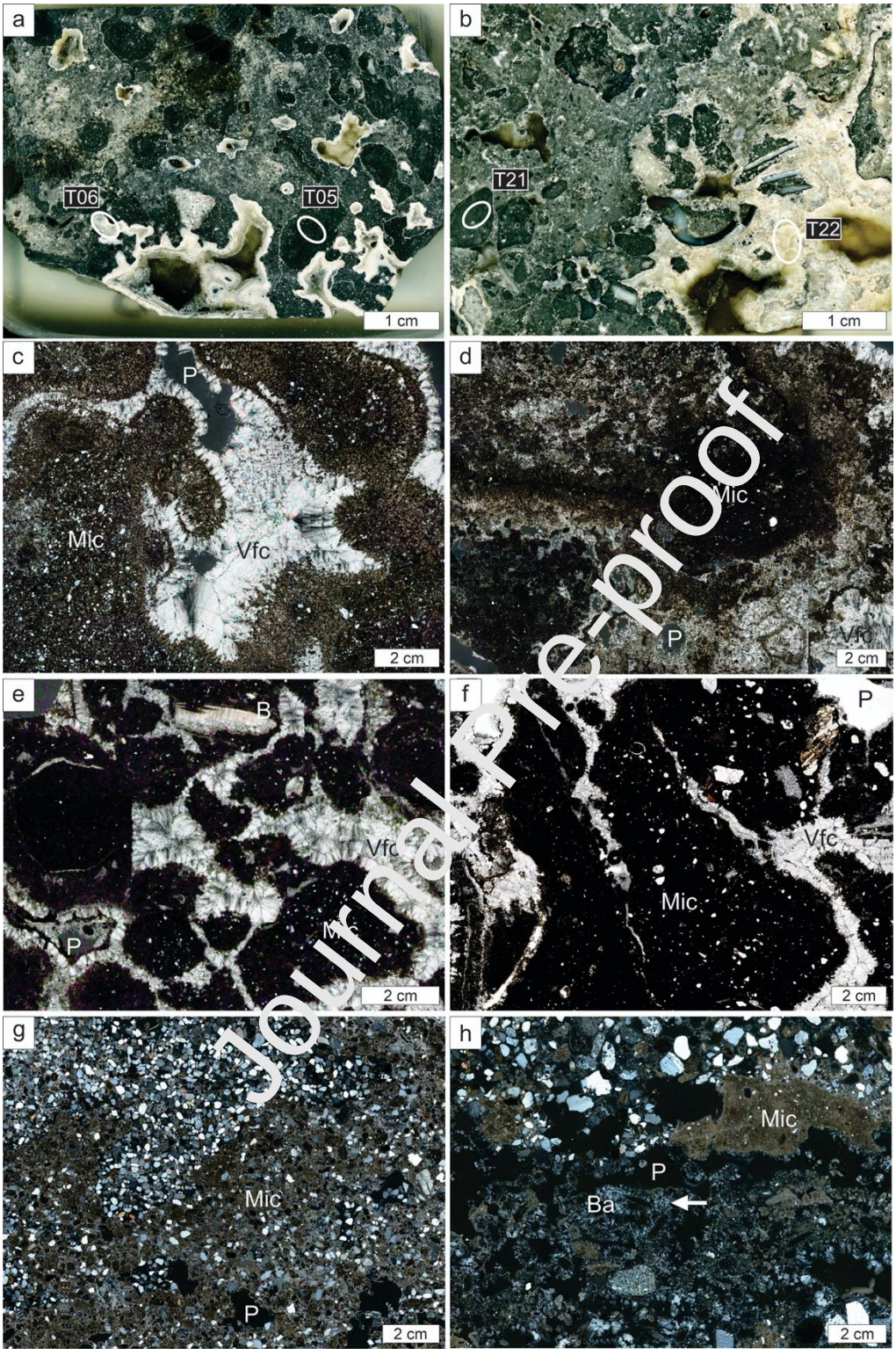

Fig. 3

--- two column fitting image ---

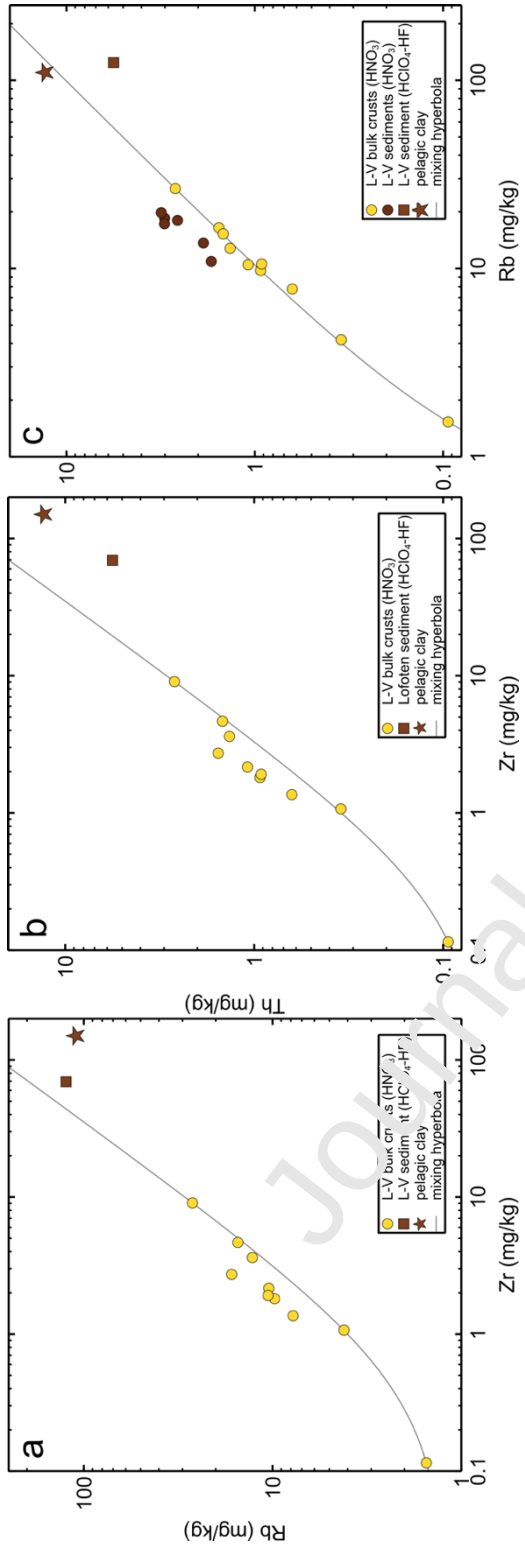

Fig. 4

--- one column fitting image ---

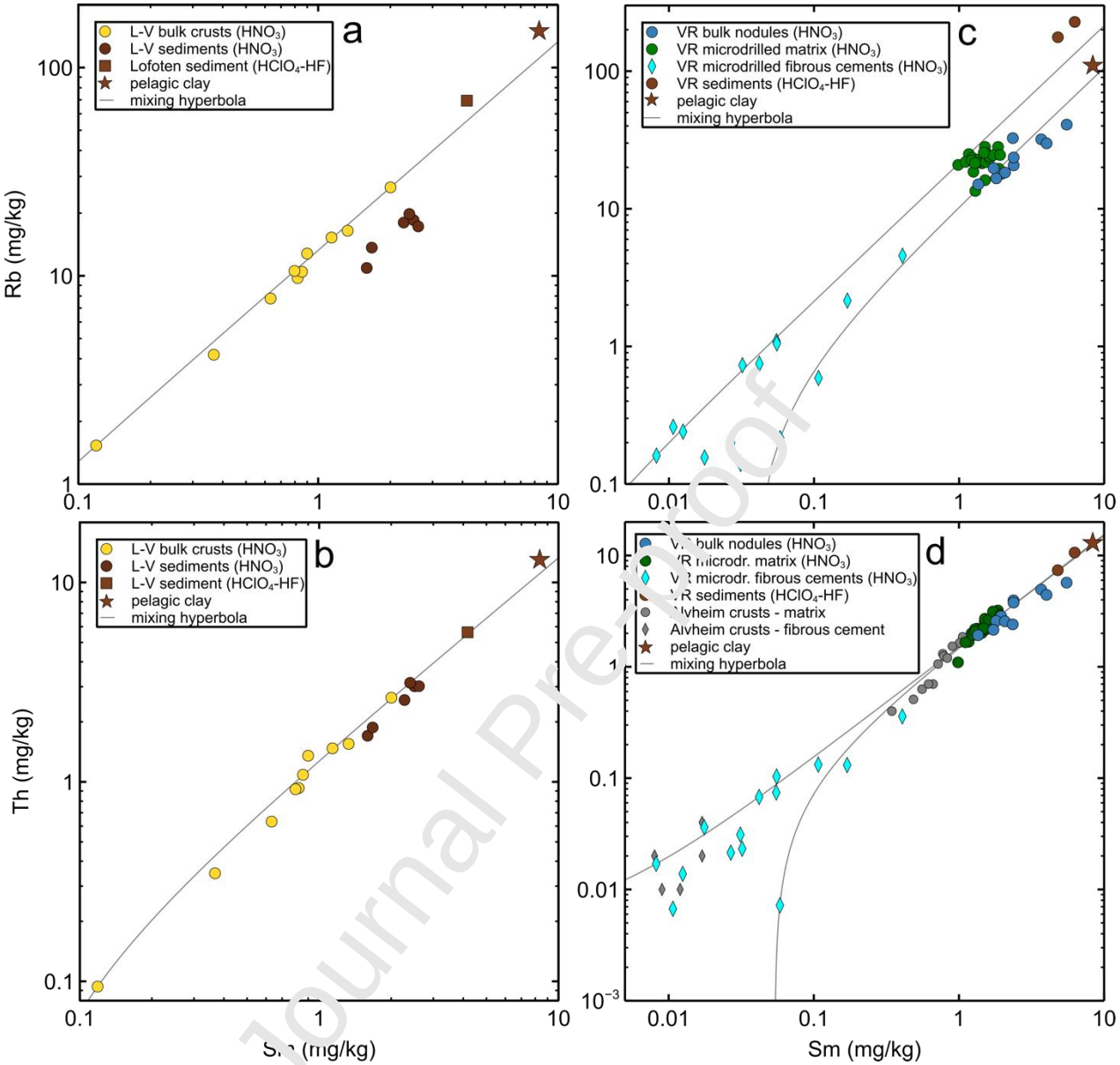

Fig. 5

--- two column fitting image ---

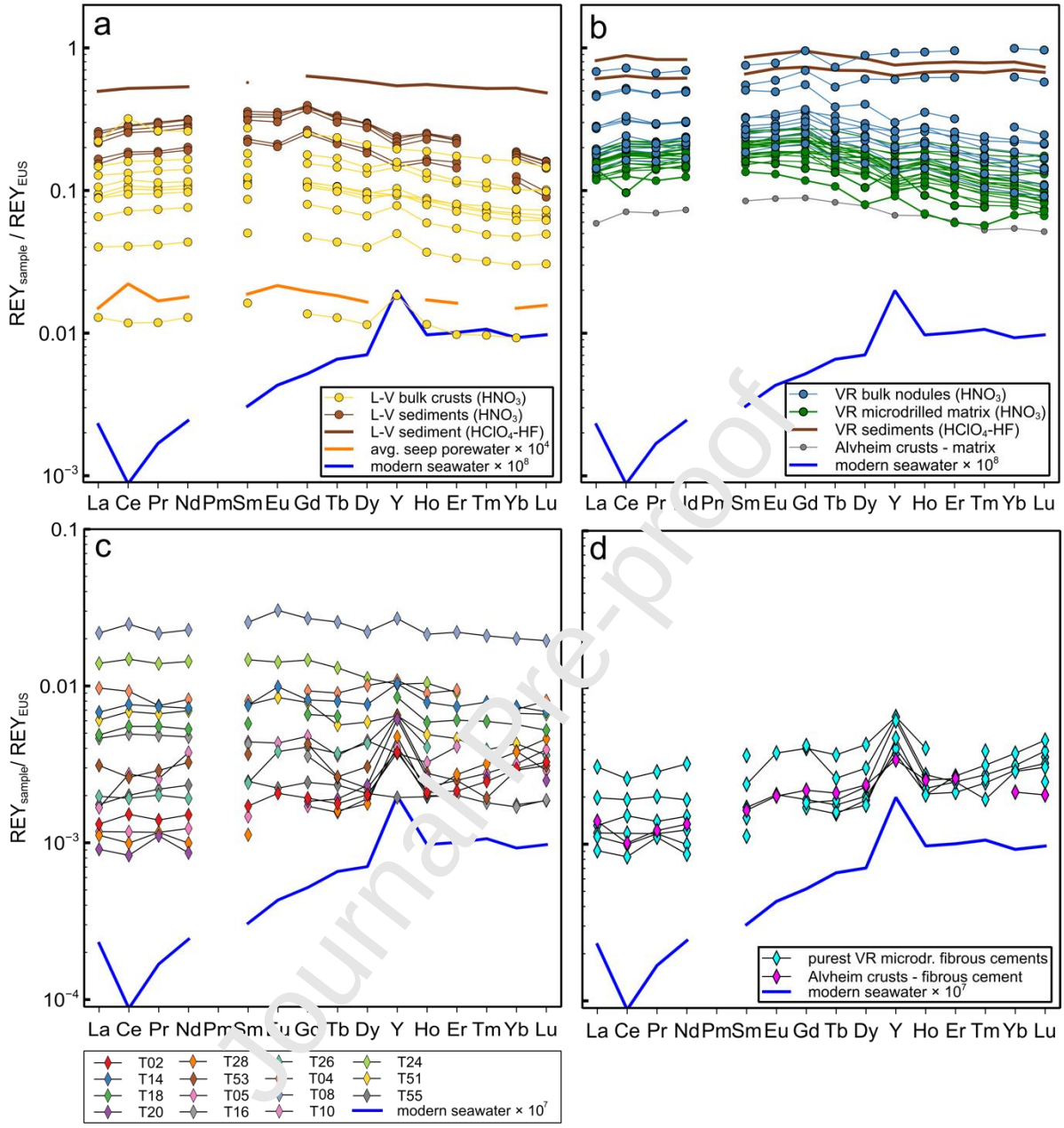

Fig. 6

--- two column fitting image ---

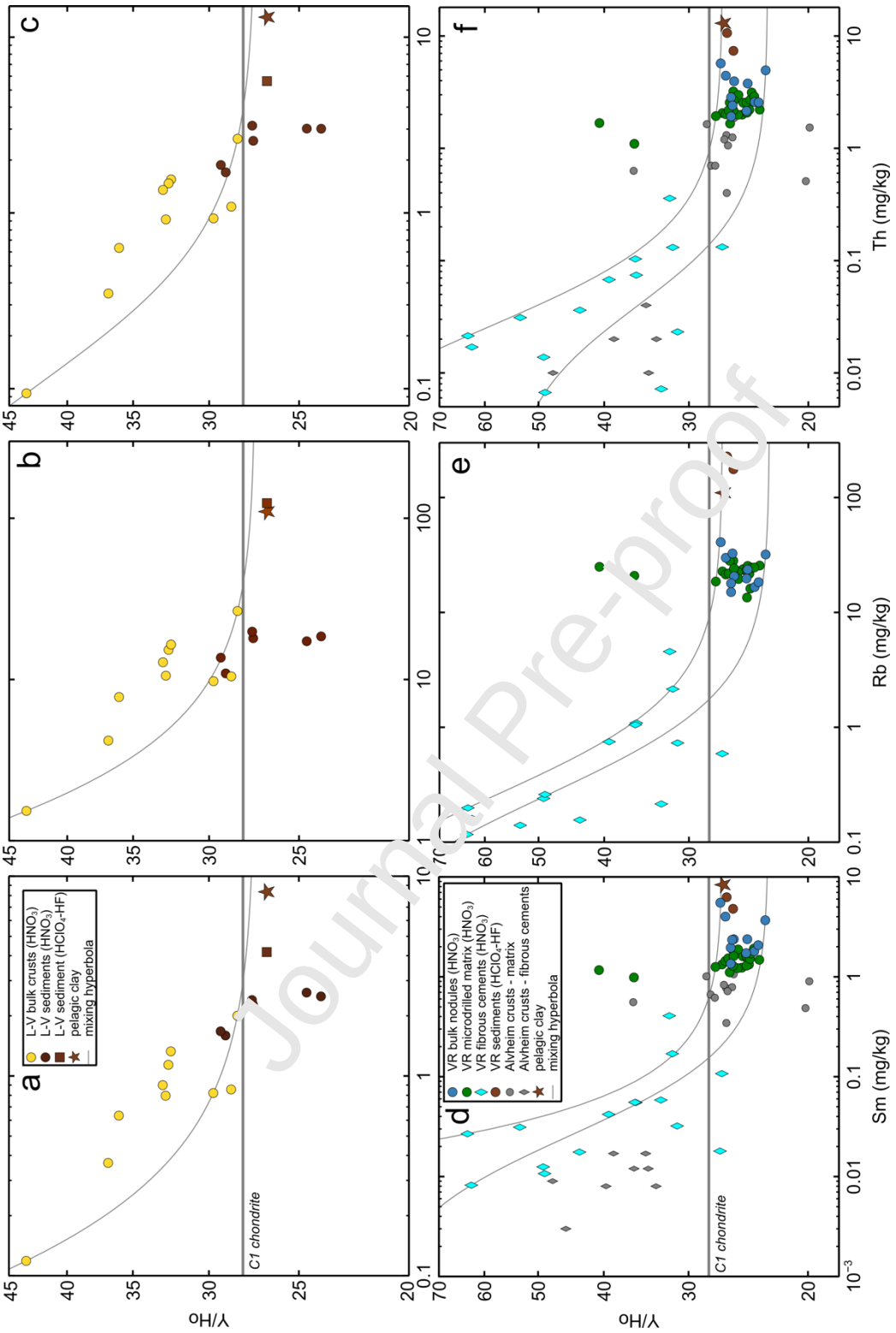

Fig. 7

--- two column fitting image ---

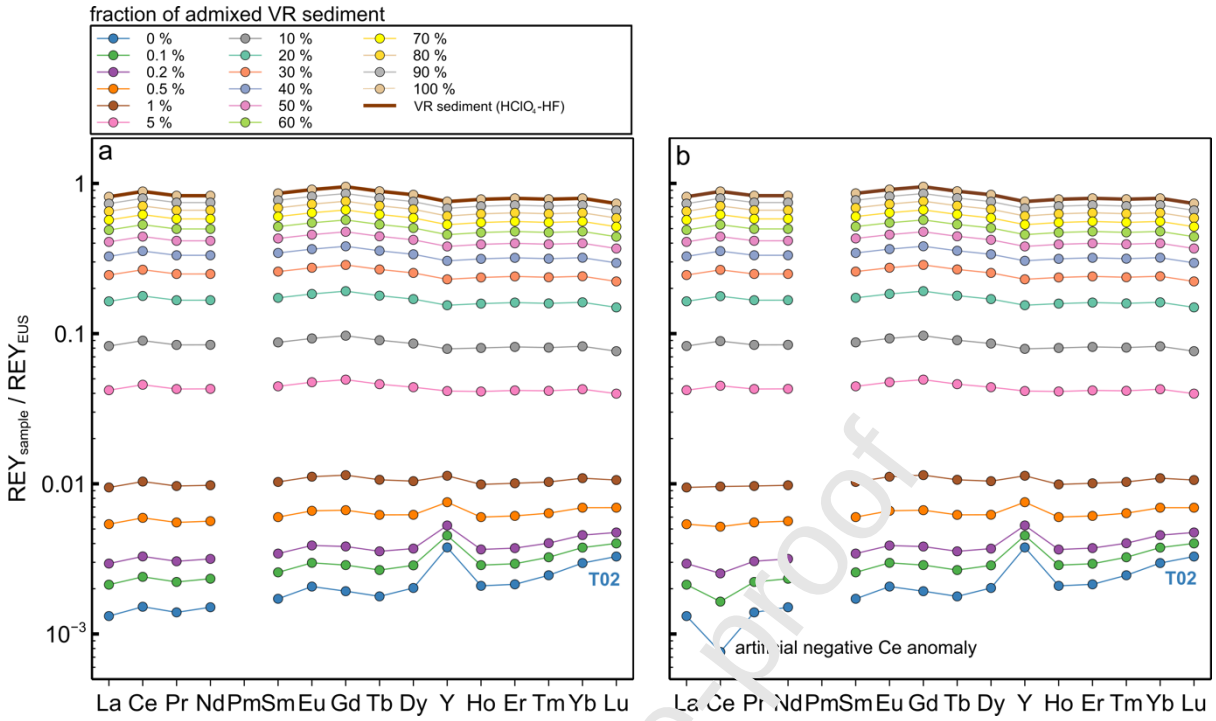

Fig. 8

--- two column fitting image ---

Table 1: Overview of all sample locations and sample types from the Lofoten-Vesterålen site and the Vestnesa Ridge, and relevant trace element concentrations discussed in this study. Trace element concentrations are given in mg/kg; Y/Ho is given as weight ratio. MCS = microcrystalline carbonate cementing sediment; Vfc = void-filling cement.

Location	Sample/core	Lab ID	Sample type	Latitude (°N)	Longitude (°E)	Sampling device	Sample depth (mbsf)	Remarks	Rb (mg/kg)	Zr (mg/kg)	Th (mg/kg)	Sm (mg/kg)	Y/Ho	∑ REY (mg/kg)
Lofoten-Vesterålen	P1710-001	n.a.	bulk crust	68° 9' 30.6"	10° 27' 39.24"	ROV	seafloor sample	MCS	[illegible].76	1.81	0.931	0.821	29.7	23.9
Lofoten-Vesterålen	P1710-003	n.a.	bulk crust	68° 9' 29.88"	10° 27' 38.88"	ROV	seafloor sample	MCS	10.[illegible]	2.16	1.09	0.856	28.7	25.0
Lofoten-Vesterålen	P1710-004	n.a.	bulk crust	68° 9' 30.24"	10° 27' 38.88"	ROV	seafloor sample	MCS	[illegible].18	1.07	0.348	0.367	36.8	10.4
Lofoten-Vesterålen	P1710-038	n.a.	bulk crust	68° 9' 28.8"	10° 27' 57.60"	ROV	seafloor sample	MCS	7.78	1.36	0.632	0.633	36.0	17.6
Lofoten-Vesterålen	P1710-039	n.a.	bulk crust	68° 9' 28.8"	10° 27' 57.24"	ROV	seafloor sample	MCS	16.5	2.73	1.55	1.33	32.4	38.4
Lofoten-Vesterålen	P1710-042	n.a.	bulk crust	68° 9' 28.8"	10° 27' 57.24"	ROV	seafloor sample	MCS	10.6	1.91	0.918	0.797	32.8	22.8
Lofoten-Vesterålen	P1710-043	n.a.	bulk crust	68° 10' 0.12"	10° 27' 51.84"	ROV	seafloor sample	MCS	26.6	9.06	2.64	2.00	28.3	63.9
Lofoten-Vesterålen	P1710-044	n.a.	bulk crust	68° 10' 0.12"	10° 27' 52.56"	ROV	seafloor sample	MCS	12.8	3.61	1.35	0.900	32.9	27.2
Lofoten-Vesterålen	P1710-045	n.a.	bulk crust	68° 10' 0.84"	10° 27' 52.20"	ROV	seafloor sample	MCS	1.53	0.115	0.0941	0.119	43.5	3.2
Lofoten-Vesterålen	P1710-047	n.a.	bulk crust	68° 10' 0.48"	10° 27' 50.76"	ROV	seafloor sample	MCS	15.3	4.66	1.47	1.14	32.6	33.0
Lofoten-Vesterålen	P1710-056	7	sediment	68° 10' 1.56"	10° 28' 12.72"	Push core	0.07	Silty clay	10.9	-	1.70	1.59	25.2	42.6
Lofoten-Vesterålen	P1710-056	10	sediment	68° 10' 1.56"	10° 28' 12.72"	Push core	0.10	Silty clay	13.7	-	1.87	1.67	25.6	44.9
Lofoten-Vesterålen	P1710-056	11	sediment	68° 10' 1.56"	10° 28' 12.72"	Push core	0.11	Silty clay	18.0	-	2.57	2.27	24.6	60.8
Lofoten-Vesterålen	P1710-056	12	sediment	68° 10' 1.56"	10° 28' 12.72"	Push core	0.12	Silty clay	18.5	-	3.01	2.50	24.2	67.7
Lofoten-Vesterålen	P1710-056	13	sediment	68° 10' 1.56"	10° 28' 12.72"	Push core	0.13	Silty clay	17.3	-	3.02	2.61	24.9	69.2
Lofoten-Vesterålen	P1710-056	17	sediment	68° 10' 1.56"	10° 28' 12.72"	Push core	0.17	Silty clay	19.8	-	3.14	2.40	26.1	65.1
Lofoten-Vesterålen	P1710-016	n.a.	sediment	68° 9' 30.96"	10° 27' 21.60"	Push core	0.1	Silty clay	124	69.4	5.62	4.17	26.7	129
Location	**Sample/core**	**Lab ID**	**Sample type**	**Latitude (°N)**	**Longitude (°E)**	**Sampling device**	**Sample depth (mbsf)**	**Remarks**	**Rb (mg/kg)**	**Zr (mg/kg)**	**Th (mg/kg)**	**Sm (mg/kg)**	**Y/Ho**	**∑ REY (mg/kg)**
Vestnesa Ridge	P1606-012	T41	crust - microdrilled matrix	79°0.46′	6°53.95′	ROV	seafloor sample	MCS	21.8	3.87	2.18	1.53	26.2	38.2
Vestnesa Ridge	P1606-012	T411	crust - microdrilled matrix	79°0.46′	6°53.95′	ROV	seafloor sample	MCS	23.3	4.56	2.56	1.63	42.4	42.4
Vestnesa Ridge	P1606-013	T421	crust - microdrilled matrix	76°0' 27"	6°53' 56"	ROV	seafloor sample	MCS	19.5	5.30	2.98	1.88	48.8	48.8
Vestnesa Ridge	P1606-014	T431	crust - microdrilled matrix	79°0' 27"	6°53' 55"	ROV	seafloor sample	MCS	13.5	2.70	2.08	1.29	32.6	32.6
Vestnesa Ridge	P1606-023	T441	crust - microdrilled matrix	79°0.41′	6°54.07′	ROV	seafloor sample	MCS	16.1	5.26	2.71	1.51	41.1	41.1
Vestnesa Ridge	P1606-012	T50	crust - microdrilled matrix	79°0.46′	6°53.95′	ROV	seafloor sample	MCS	24.2	6.87	2.66	1.61	43.0	43.0
Vestnesa Ridge	P1606-023	T52	crust - microdrilled matrix	79°0.41′	6°54.07′	ROV	seafloor sample	MCS	24.5	6.95	3.14	1.72	46.8	46.8
Vestnesa Ridge	P1606-002	T54	crust - microdrilled matrix	79°0.16′	6°55.28′	ROV	seafloor sample	MCS	25.6	5.59	2.21	1.48	40.5	40.5
Vestnesa Ridge	P1606-013	T56	crust - microdrilled matrix	76° 0' 27"	6° 53' 56"	ROV	seafloor sample	MCS	24.6	6.10	2.89	1.92	50.0	50.0

Vestnesa Ridge	P1606-009	PC01	bulk nodule	79° 0' 9"	6° 55' 19"	Push core	0.13-0.16	MCS nodule	17.9	4.15	2.85	1.95	25.7	52.6
Vestnesa Ridge	P1606-009	PC02	bulk nodule	79° 0' 9"	6° 55' 19"	Push core	0.16-0.18	MCS nodule	16.6	3.94	2.58	1.80	25.5	49.2
Vestnesa Ridge	P1606-009	PC03	bulk nodule	79° 0' 9"	6° 55' 19"	Push core	0.18-0.20	MCS nodule	18.3	3.57	2.56	2.07	23.7	55.7
Vestnesa Ridge	P1606-009	PC04	bulk nodule	79° 0' 9"	6° 55' 19"	Push core	0.20-0.23	MCS nodule	19.7	4.10	2.15	1.73	24.7	46.6
Vestnesa Ridge	P1606-009	PC05	bulk nodule	79° 0' 9"	6° 55' 19"	Push core	0.23-0.26	MCS nodule	15.0	3.71	1.92	1.35	25.8	38.5
Vestnesa Ridge	P1606-017	PC06	bulk nodule	79° 0' 28"	6° 53' 58"	Push core	0.41-0.43	MCS nodule	32.6	5.29	2.41	2.35	25.9	74.0
Vestnesa Ridge	GeoB21609-1	T33	bulk nodule	79°0.41'	6°54.27'	Gravity core	4.60-4.80	MCS nodule, GC-4	20.7	6.35	3.95	2.38	25.7	71.8
Vestnesa Ridge	GeoB21609-1	T34	bulk nodule	79°0.41'	6°54.27'	Gravity core	5.20-5.30	MCS nodule, GC-4	31.9	3.54	4.95	3.68	23.1	113
Vestnesa Ridge	GeoB21605-1	T35	bulk nodule	79°0.51'	6°54.61'	Gravity core	7.04	MCS nodule, GC-2	23.6	8.17	3.78	2.38	24.6	71.9
Vestnesa Ridge	GeoB21605-1	T36	bulk nodule	79°0.51'	6°54.61'	Gravity core	7.04	MCS nodule, GC-2	2[illegible]9	5.79	4.43	4.01	26.5	130
Vestnesa Ridge	GeoB21605-1	T38	bulk nodule	79°0.51'	6°54.61'	Gravity core	7.50	MCS nodule, GC-2	[illegible]0.9	6.50	5.70	5.52	26.9	186
Vestnesa Ridge	GeoB21616-1	T01	crust - microdrilled matrix	79°0.43′	6°54.25′	MeBo core 127	5.75	MCS	25.0	6.0	1.68	1.17	40.7	30.1
Vestnesa Ridge	GeoB21616-0	T03	crust - microdrilled matrix	79°0.43′	6°54.25′	MeBo core 127	5.75	MCS	20.8	5.65	1.10	0.985	36.1	28.6
Vestnesa Ridge	GeoB21616-1	T06	crust - microdrilled matrix	79°0.43′	6°54.25′	MeBo core 127	5.75	MCS	28.1	6.54	3.21	1.86	25.8	53.3
Vestnesa Ridge	GeoB21616-1	T07	crust - microdrilled matrix	79°0.43′	6°54.25′	MeBo core 127	5.75	MCS	28.2	6.04	2.56	1.51	26.1	42.8
Vestnesa Ridge	GeoB21616-1	T09	crust - microdrilled matrix	79°0.43′	6°54.25′	MeBo core 127	10.72	MCS	23.5	5.37	1.99	1.23	25.0	35.0
Vestnesa Ridge	GeoB21637-1	T23	crust - microdrilled matrix	79°0.43′	6°54.25′	MeBo core 138	16.[illegible]5	MCS	18.6	5.77	1.94	1.26	27.4	41.5
Vestnesa Ridge	GeoB21637-1	T13	crust - microdrilled matrix	79°0.43′	6°54.25′	MeBo core 138	19.25	MCS	22.7	7.26	2.06	1.33	26.8	41.3
Vestnesa Ridge	GeoB21637-1	T15	crust - microdrilled matrix	79°0.43′	6°54.25′	MeBo core 138	21.73	MCS	21.9	4.99	1.66	1.11	26.1	32.9
Vestnesa Ridge	GeoB21637-1	T17	crust - microdrilled matrix	79°0.43′	6°54.25′	MeBo core 138	21.73	MCS	23.8	4.80	2.55	1.60	25.0	47.6
Vestnesa Ridge	GeoB21637-1	T19	crust - microdrilled matrix	79°0.43′	6°54.25′	MeBo core 138	21.73	MCS	22.4	5.17	1.99	1.22	25.4	36.4
Vestnesa Ridge	GeoB21637-1	T21	crust - microdrilled matrix	79°0.43′	6°54.25′	MeBo core 138	21.73	MCS	21.4	5.08	2.01	1.44	26.5	44.8
Vestnesa Ridge	GeoB21637-1	T25	crust - microdrilled matrix	79°0.43′	6°54.25′	MeBo core 138	21.73	MCS	25.4	5.57	2.17	1.53	24.6	45.2
Vestnesa Ridge	GeoB21637-1	T27	crust - microdrilled matrix	79°0.43′	6°54.25′	MeBo core 138	21.73	MCS	21.7	5.13	2.20	1.33	24.4	37.4
Vestnesa Ridge	GeoB21637-1	T30	crust - microdrilled matrix	79°0.43′	6°54.25′	MeBo core 138	21.73	MCS	21.5	4.88	2.18	1.29	25.8	35.2
Vestnesa Ridge	P1606-012	T51	crust - microdrilled fibrous cement	79°0.43′	06°53.95′	ROV	seafloor sample	Vfc	1.05	0.330	0.104	0.0554	36.0	1.62
Vestnesa Ridge	P1606-023	T53	crust - microdrilled fibrous cement	79°0.41′	06°54.07′	ROV	seafloor sample	Vfc	0.199	0.198	0.0214	0.0268	63.5	0.833
Vestnesa Ridge	P1606-022	T55	crust - microdrilled fibrous cement	79° 0' 23"	6° 53' 56"	ROV	seafloor sample	Vfc	-	-	-	0.0180	27.0	0.500
Vestnesa Ridge	GeoB21616-1	T04	crust - microdrilled fibrous cement	79°0.42′	6°54.26′	MeBo core 127	5.75	Vfc	0.215	0.179	0.00725	0.0584	33.0	2.27
Vestnesa Ridge	GeoB21616-1	T05	crust - microdrilled fibrous cement	79°0.42′	6°54.26′	MeBo core 127	5.75	Vfc	0.260	0.307	0.00672	0.0107	48.9	0.406
Vestnesa Ridge	GeoB21616-1	T08	crust - microdrilled fibrous cement	79°0.42′	6°54.26′	MeBo core 127	5.75	Vfc	2.15	0.865	0.131	0.170	31.7	4.27
Vestnesa Ridge	GeoB21616-1	T02	crust - microdrilled fibrous cement	79°0.42′	6°54.26′	MeBo core 127	5.75	Vfc	0.240	0.416	0.0138	0.0125	49.1	0.451
Vestnesa Ridge	GeoB21616-1	T10	crust - microdrilled fibrous cement	79°0.42′	6°54.26′	MeBo core 127	10.27	Vfc	0.730	0.184	0.0232	0.0321	31.2	0.741
Vestnesa Ridge	GeoB21637-1	T24	crust - microdrilled fibrous cement	79°0.43′	6°54.26′	MeBo core 138	16.95	Vfc	0.589	0.244	0.132	0.107	26.8	3.34

Vestnesa Ridge	GeoB21637-1	T14	crust - microdrilled fibrous cement	79°0.43′	6°54.26′	MeBo core 138	19.25	Vfc	1.09	0.420	0.0743	0.0551	35.9	1.91
Vestnesa Ridge	GeoB21637-1	T18	crust - microdrilled fibrous cement	79°0.43′	6°54.26′	MeBo core 138	21.73	Vfc	0.748	0.404	0.0677	0.0420	39.3	1.38
Vestnesa Ridge	GeoB21637-1	T20	crust - microdrilled fibrous cement	79°0.43′	6°54.26′	MeBo core 138	21.73	Vfc	0.117	0.135	-	-	63.8	0.387
Vestnesa Ridge	GeoB21637-1	T28	crust - microdrilled fibrous cement	79°0.43′	6°54.26′	MeBo core 138	21.73	Vfc	0.161	0.398	0.0170	0.00821	62.7	0.389
Vestnesa Ridge	GeoB21637-1	T16	crust - microdrilled fibrous cement	79°0.43′	6°54.26′	MeBo core 138	21.73	Vfc	0.140	0.187	0.0311	0.0312	53.2	1.09
Vestnesa Ridge	GeoB21637-1	T26	crust - microdrilled fibrous cement	79°0.43′	6°54.26′	MeBo core 138	21.73	Vfc	0.156	0.309	0.0362	0.0176	43.4	0.649
Vestnesa Ridge	GeoB21601-1	M1	sediment	79°0.50′	6°54.64′	Gravity core	0.04	Silty clay; station GC-1	228	151	10.6	6.27	26.4	206
Vestnesa Ridge	GeoB21637-1	M6025	sediment	79°0.43′	6°54.26′	MeBo core 138	15.11	Silty clay	76	159	7.38	4.80	25.8	156

Declaration of competing interests

☒ The authors declare that they have no known competing financial interests or personal relationships that could have appeared to influence the work reported in this paper.

☐The authors declare the following financial interests/personal relationships which may be considered as potential competing interests:

HIGHLIGHTS

- screening procedure to study REY geochemistry of seep carbonate crusts
- trace element leaching from silicates of carbonate crusts during HNO_3 digestion
- masking of authigenic carbonate REY signal
- void-filling cements are reliable archives of REY in carbonate-precipitating fluid
- seawater-like REY_{SN} patterns in purest void-filling cements